Competence for transcellular infection in the root cortex involves a post-replicative, cell-cycle exit decision in *Medicago truncatula*.

Morgane Batzenschlager[1,*], Beatrice Lace[1], Ning Zhang[1,2], Chao Su[1], Sabrina Egli[1], Pascal Krohn[1,3], Jule Salfeld[1], Franck Anicet Ditengou[1,4], Thomas Laux[1,2], and Thomas Ott[1,2,*].

[1] *University of Freiburg, Faculty of Biology, 79104 Freiburg, Germany*

[2] *CIBSS – Centre of Integrative Biological Signalling Studies, University of Freiburg, Freiburg, Germany*

[3] *present address: Max Planck Institute for Plant Breeding Research, Department for Plant-Microbe Interactions, 50829 Cologne, Germany*

[4] *present address: Freiburg University Medical Centre, Institute for Disease Modelling and Targeted Medicine (IMITATE), 79106 Freiburg, Germany*

*Corresponding authors:

morgane.batzenschlager@biologie.uni-freiburg.de; thomas.ott@biologie.uni-freiburg.de

ABSTRACT

During root nodule symbiosis (RNS), cell-division activity is re-initiated and sustained in the root cortex to create a hospitable cellular niche. Such temporary and spatially confined site is required to render host cells compatible with the intracellular progression of rhizobia. Although it has been suggested that early infection events might involve a pre-mitotic cell-cycle arrest, this process has not been dissected with cellular resolution. Here, we show that a dual-colour Medicago histone reporter robustly identifies cells with different mitotic or endoreduplication activities in the root cortex. By imaging deep root tissues, we found that a confined trajectory of cortical cells that are

transcellularly passed by infection threads are in a stage of the cell-cycle that is distinct from directly adjacent cells. Distinctive features of infected cells include nuclear widening and large-scale chromatin rearrangements consistent with a cell-cycle exit prior to differentiation. Using a combination of fluorescent reporters demarcating cell-cycle phase progression, we confirmed that a reduced proliferation potential and modulating the G2/M transition, a process possibly controlled by the NF-YA1 transcription factor, mark the success of rhizobial delivery to nodule cells.

INTRODUCTION

Cell-cycle regulation is a key pathway to maintain beneficial and sustainable symbiotic associations that are of primary importance in both marine and terrestrial ecosystems. One common theme to stabilize facultative associations is to achieve a mutual control of cell proliferation and differentiation dynamics in both the host and the symbionts (Kondorosi & Kondorosi, 2004; Russo & Genre, 2021). Prime examples are flowering plants from a single phylogenetic clade, comprising four orders (Fabales, Fagales, Cucurbitales, Rosales) with legumes being the most prominent ones, that evolved the unique ability to accommodate soil-borne rhizobia intracellularly (Parniske, 2018). Within this symbiosis, rhizobia fix atmospheric nitrogen and deliver ammonium to the host in exchange for plant photosynthates. The conversion of atmospheric dinitrogen into a usable form is highly energy-demanding and requires a low-oxygen environment, which is provided within nodules, specialized lateral organs formed on the roots that are densely populated by rhizobia. A widely adopted mechanism to access the developing nodule cells is the formation of cortical infection threads, transcellular conduits formed upon the invagination of the host plasma membrane and hijacking the cellular machinery of infected root cortical cells (Timmers et al., 1999; Su et al., 2023). Although our molecular and cellular understanding of the infection mechanisms is expanding (Tsyganova et al., 2021), our knowledge on how these processes are interconnected with the control of cell-cycle progression in cells hosting intracellular infection threads has remained fragmentary.

51 Plants engaging into arbuscular mycorrhizal (AM) or root nodule symbioses (RNS) have
52 recruited a common range of cell-cycle processes (Foucher & Kondorosi, 2000; Russo & Genre,
53 2021). In *Medicago truncatula* (hereafter, Medicago), the perception of and colonization by the AM
54 fungus result in occasional cell divisions in the inner cortical layers (Russo et al., 2019) and in diffuse
55 endoreduplication events as intraradical hyphae spread throughout the root cortex (Carotenuto et al.,
56 2019a; Carotenuto et al., 2019b). During RNS, the perception of rhizobia results in the onset of a
57 signalling cascade that triggers an outward gradient of cell-cycle reactivation and cell divisions.
58 Although this is initiated in the pericycle, cell-cycle reactivation occurs throughout the inner cortical
59 (C) layers C5, C4 and the middle C3 layer in Medicago (Timmers et al., 1999; Xiao et al., 2014). The
60 successful establishment of RNS further involves the tight coordination of the infection and
61 organogenesis programmes (Guan et al., 2013). It requires the progression of cortical infection
62 threads through the C3 layer prior to subsequent periclinal divisions that produce a persistent nodule
63 meristem (Xiao et al., 2014). The resulting indeterminate nodules will later form well-defined
64 developmental zones, with actively dividing meristematic cells giving rise to post-meristematic,
65 differentiating central tissues of increasing ploidy (Vinardell et al., 2003; Nagymihály et al., 2017).
66 While those cells can be intracellularly colonized, the infection competence of nodule-like structures
67 as being induced by exogenous application of cytokinin (Gauthier-Coles et al., 2019), constitutive
68 activation of common symbiotic components (Gleason et al., 2006; Singh et al., 2014) or the
69 expression of meristematic factors (Dong et al., 2021) may be massively reduced in many of these
70 spontaneous nodules (Hayashi et al., 2010; Liu et al., 2022). The lack of infectibility cannot be
71 overcome even when applying bacterial strains which enter plant cells from the intercellular space
72 (Liang et al., 2019). This clearly demonstrates the ultimate requirement of cells being in a so far
73 uncharacterized state of infection competence.

74 Transcriptome profiling of Medicago root hairs, treated with rhizobial Nod factors or
75 undergoing rhizobial colonization, uncovered changes in several cell-cycle related genes (Breakspear
76 et al., 2014; Liu et al., 2019a). This perception of Nod factors results in the increased transcription of

77 D-type cyclins, genes known to respond to extrinsic signals and to promote cell-cycle progression
78 from the first GAP (G1) phase to the DNA-synthesis (S) phase (Dewitte et al., 2003). Subsequently,
79 the initiation of infection threads coincides with the highest expression of genes required for DNA
80 replication, modification and repair, strongly suggesting that the epidermal infection programme
81 involves cell cycle re-entry and progression to a post-replicative phase (Breakspear et al., 2014). A
82 repression of the endocycle was further proposed to occur since infected root hairs accumulate
83 transcripts of the *OSD1/UVI4* gene (Breakspear et al., 2014), whose activity prevents an unscheduled
84 increase in ploidy by inhibiting the anaphase-promoting complex/cyclosome (Iwata et al., 2011).
85 However, much less is known about the transcriptional signature of infected cells along the cortical
86 trajectory of transcellularly progressing infection threads. Such ability to guide rhizobia *via* cortical
87 infection threads is yet thought to be an important innovation since it has been evolutionary
88 maintained in the vast majority of nodulating species as it, most likely, maximizes the host control
89 over bacterial delivery (Parniske, 2018; Cathebras et al., 2022 – pre-print).

90 A central regulator for controlling infection and organogenesis is the transcription factor
91 *Nodule Inception* (*NIN*). Co-opted from nitrate response circuits, NIN acts as a master coordinator of
92 infection, nodule organogenesis and nodule number (Marsh et al., 2007; Fournier et al., 2015; Soyano
93 et al., 2014; Cathebras et al., 2022 – pre-print). It promotes the expression of several growth targets
94 (Liu et al., 2019a) including *NF-YA1* (Soyano et al., 2013; Feng et al., 2021), a subunit of the
95 conserved heterotrimeric Nuclear Factor-Y (NF-Y) transcription factor. A-, B- and C-type subunits
96 of the NF-Y complex act as specialized modules, interacting with other transcription factors and
97 recruiting chromatin remodelling enzymes to adjust cell specification to environmental or
98 developmental needs (Zanetti et al., 2016; Myers & Holt, 2018). In vertebrates, the CCAAT-binding
99 NF-Y transcription factor targets genes involved in all major activities executed in G2 and mitosis
100 (M; Linhart et al., 2005) and is an important regulator of the G2/M transition (Manni et al., 2001). In
101 legumes, the rhizobium-induced NF-YA1 subunit functions in cortical infection thread progression,
102 in the establishment and maintenance of the nodule meristem and in the early differentiation of nodule

103 cells (Combier et al., 2006; Laporte et al., 2014; Xiao et al., 2014; Hossain et al., 2016; Schiessl et
104 al., 2023 – pre-print). Yet, whether the Medicago NF-YA1 protein regulates the G2/M transition is
105 not known.

106 The hypothesis that intracellular infection at least partially relies on cell-cycle control is
107 further supported by structural re-arrangements in cortical cells anticipating transcellular IT
108 progression. These include the formation of pre-infection threads (PITs), which are transvacuolar,
109 cytoplasmic bridges comparable to those occurring in pre-mitotic cells (van Brussel et al., 1992;
110 Timmers et al., 1999). *In situ* detection of marker transcripts revealed that outer cortical cells recruit
111 histone H4 used during DNA replication but do not express a B-type, mitotic cyclin gene – implying
112 that activated target cells stop in the G2 phase of the cell cycle (Yang et al., 1994). G2-phase cell-
113 cycle arrests have been repeatedly described in eukaryotic cells as appropriate gates for executing
114 cell fate and patterning decisions (Meserve & Duronio, 2017), for wound healing (Cosolo et al., 2019)
115 or for host infection during pathogenic and biotrophic interactions (Wildermuth et al., 2017). In
116 plants, transiently or sustainably reducing the potential to enter mitosis is an appropriate response
117 when cells must, for instance, cope with genotoxic stresses (Chen et al., 2017; Takahashi et al., 2019)
118 or switch to another cell-cycle program, such as the meiotic (Hernandez-Lagana et al., 2021) or the
119 endoreduplication cycle (De Veylder et al., 2011; Wildermuth et al., 2017). Modulating the G2/M
120 transition combines well-described transcriptional and post-translational mechanisms, leading to the
121 repression of genes necessary to execute cell division (Berckmans & De Veylder, 2009; Kobayashi
122 et al., 2015), controlling the activity of cyclin-dependent kinases (CDK) and the stability of
123 transcriptional repressors and mitotic inducers (Kondorosi & Kondorosi, 2004; Chen et al., 2017).
124 Although previous reports have suggested such cell-cycle patterns to occur in roots during rhizobial
125 infections (Yang et al., 1994; Breakspear et al., 2014), this has never been spatially resolved at cellular
126 level.

127 Here, we employed a combination of cell-cycle reporters to resolve functional steps of cell-
128 cycle progression on the cortical infection thread trajectory with cellular and subcellular resolution.

129 We demonstrate that the first generation of Medicago cells successfully internalizing rhizobia shows
130 unique features, including a marked decrease in their histone H3.1 content and a reduced competence
131 for both cell division and chromosome segregation. We also show that tetraploid (4n) cells reaching
132 an 8C DNA content are optimal for infection by rhizobia. Our results strongly suggest that, upon
133 transcellular infection thread passage, cortical cells undergo a last GAP phase after DNA replication
134 and exit to differentiation. Furthermore, we present first evidence that the symbiotically-induced NF-
135 YA1 subunit, by controlling mitotic entry in a heterologous system, holds potential to contribute to
136 this process.
137

138 **RESULTS**

139 ***A reduced proliferative potential typifies cells supporting cortical infection thread progression***

140 In *Arabidopsis thaliana* (hereafter, Arabidopsis), the incorporation and eviction dynamics of histone
141 H3 variants have been used to identify cells with different cell division and reprogramming potentials,
142 during organ patterning (Otero et al., 2016) or when acquiring reproductive competence (Hernandez-
143 Lagana & Autran, 2020). To test whether gaining a stage of intracellular infection competence
144 involves a similar modification of the cell-division potential and associated chromatin reorganization,
145 we searched for Medicago genes coding for the replicative histone variant H3.1 and the replacement
146 variant H3.3 (Figure 1–figure supplement 1A; Probst et al., 2020). The encoded Medicago H3.1
147 protein is identical to the one present in *Lotus japonicus* and *Hordeum vulgare* and, as in other
148 flowering plants, differs from H3.3 by only four residues (Figure 1–figure supplement 1B; Shi et al.,
149 2011). To check that these Medicago *H3* genes encode for *bona fide* H3.1 and H3.3 counterparts,
150 native promoter-genomic fusions with fluorescent tags were expressed in *Agrobacterium rhizogenes*–
151 induced transgenic roots, formed on composite plants that were inoculated with the compatible
152 symbiont *Sinorhizobium meliloti* (each composite plant representing an independent transformant;
153 Boisson-Dernier et al., 2001). We adopted a fixation, clearing and cell-wall counter-staining
154 procedure (Ursache et al., 2018) that enabled us to perform detailed imaging deep inside the multi-

155 layered root cortical tissues. Medicago H3 fusion proteins fully recapitulated the patterns observed in
156 Arabidopsis roots (*i.e.,* patchy pattern of H3.1 and constitutive presence of H3.3; Figure 1–figure
157 supplement 1C–E) and showed the expected localization in euchromatin (diffuse labelling) and
158 heterochromatic regions (subnuclear foci; Figure 1–figure supplement 1C–E; Ingouff et al., 2010; Shi
159 et al., 2011; Otero et al., 2016). A low H3.1 content, typical for cells with a reduced proliferative
160 potential, also enabled us to identify putative quiescent centre (QC) cells within the open root apical
161 meristem of Medicago (Figure 1–figure supplement 1E; Rost, 2011; Otero et al., 2016; Xiao et al.,
162 2019). Preferentially incorporated during DNA replication, the canonical histone H3.1 variant
163 controls the maintenance of genome integrity (Davarinejad et al., 2022) and epigenetic inheritance
164 (Jiang & Berger, 2017) and is consequently maintained at high levels in cells engaged in recurrent
165 cell division or endoreduplication cycles (Figure 1A). Once cells exit the cell cycle, H3.1 is evicted
166 and likely replaced by H3.3 to mediate cellular differentiation in various Arabidopsis cell types (Otero
167 et al., 2016). In Medicago, increased levels of *H3.1* transcripts were coherently detected at an early
168 stage of nodule primordia development (Figure 1– figure supplement 1F; Schiessl et al., 2019) and
169 mRNAs accumulated only in meristematic (ZI) and infection zones of mature nodules (ZIId and ZIIp;
170 Roux et al., 2014), while *H3.3* transcription stayed high in the differentiation zone (ZIII; Figure 1–
171 figure supplement 1G). We verified a corresponding differential accumulation of H3.1 and H3.3
172 tagged proteins at cellular resolution in nodule sections (Figure 1B). The double histone reporter
173 proved also useful to distinguish actively endoreduplicating cells prior to fungal colonization
174 (Carotenuto et al., 2019a; Carotenuto et al., 2019b) from fully differentiated, arbuscule-containing
175 cells (Figure 1C). Since the selected Medicago histone variants recapitulated the expected
176 transcriptional and localization patterns in well-defined developmental zones, we considered them as
177 functional reporters of H3.1 and H3.3. In addition, the H3.1/H3.3 balance enables to track cortical
178 cells re-entering the cell cycle and adapting their responses to both bacterial and fungal symbionts.

179 We then focused on the H3.1 nuclear content at early interaction stages between rhizobia and
180 the host plant (8 days post inoculation [dpi]; Figure 2A–B). In accordance with RNA sequencing data

181 (Figure 1– figure supplement 1F; Schiessl et al., 2019), we observed the replicative H3.1 variant
182 accumulating in regularly dividing cortical cells forming the nodule primordium (Figure 2A, left
183 panel). The H3.1-eGFP fusion protein was also visible in cells penetrated but not fully passed by an
184 infection thread (Figure 2A, close up). This is consistent with earlier observations that cells preparing
185 for intracellular infection pass through S-phase (Yang et al., 1994). By contrast, host cells sustaining
186 cortical infection thread progression in the middle and inner cortex (C3 and C4) up to the first
187 recipient cells in the nodule primordium (C4/5-derived; Figure 2B) exhibited enlarged nuclei (Figure
188 2C) with a significantly decreased histone H3.1 content compared to their direct neighbouring cells
189 (Figure 2D). Such pattern was also observed using another *H3.1* gene expressed in root tissues (*H3.1*
190 *(2)*; Figure 2–figure supplement 1A–E). Nuclear enlargement associated with a massive eviction of
191 H3.1 typically identifies cells having completed a DNA replication round, but pausing in the
192 following GAP phase for cell-cycle switches or exit decisions (Figure 2E; Otero et al., 2016;
193 Hernandez-Lagana & Autran, 2020; Probst et al., 2020). Together, our data strongly suggest that
194 cortical cells along the infection thread trajectory, different to their direct neighbours, exhibit a
195 reduced proliferation potential and presumably exit the cell cycle (Figure 2 B–E). The observed
196 nuclear enlargement and large-scale chromatin rearrangements are consistent with an increased
197 transcriptional activity (Knaack et al., 2022) concomitant with sustained infection thread progression
198 (Breakspear et al., 2014; Liu et al., 2019a). This proves the long-standing hypothesis that cortical
199 cells competent for transcellular infection suspend their course in G2 (Yang et al., 1994; Timmers et
200 al., 1999) in Medicago.

201

202 ***Exiting the cell cycle on the cortical infection thread trajectory aligns infection and organogenesis***
203 Next, we tested whether a cell-cycle exit decision and associated remodelling of the histone H3
204 composition requires the tight coupling of infection and nodule organogenesis as observed under
205 wild-type (WT) conditions. Thus, we compared the H3.1/H3.3 patterns in WT roots to those of two
206 mutants in which nodule organogenesis is either abolished (*daphne-like*; Liu et al., 2019b) or where

207 nodules form but cortical infection threads are impaired in their progression (*nf-ya1-1*; Laporte et al.,
208 2014). In the WT situation, the majority of cortical cells (90%) enabling transcellular passage until
209 reaching the nodule primordium showed a reduced proliferation potential (low H3.1 content, n = 41;
210 Figure 3A and Figure 3–figure supplement 1A). A higher H3.1 content was occasionally observed in
211 the last infected cell in the absence of nodule primordium organogenesis (NOD $^{(-)}$; Figure 3–figure
212 supplement 1B). Absence of inner cortical cell division is also a characteristic feature of the *daphne-*
213 *like* Medicago mutant (Figure 3–figure supplement 1C), which lacks a remote cis-regulatory region
214 in the *NIN* promoter perceiving cytokinin signals (Liu et al., 2019b). This non-nodulating mutant still
215 produces WT-like root hair infections occasionally reaching outer cortical layers. In this context, the
216 percentage of infected cortical cells visibly accumulating H3.1 in the euchromatin increased from
217 10% in the WT to almost 41% in the *daphne-like* mutant (n = 44; Figure 3A and Figure 3–figure
218 supplement 1D). This indicates that outer cortical cells hosting an infection thread lack an extensive
219 chromatin reorganization in the absence of sustained nodule organogenesis.
220 As a second mutant, we chose a *nf-ya1* null allele, producing smaller nodules that are additionally
221 delayed and impaired in their development (Laporte et al., 2014; Xiao et al., 2014). Nodule primordia
222 of the *nf-ya1-1* mutant showed reduced cell layers, with a lower frequency of cell divisions in the
223 inner cortex (C4/5) and only few anticlinal divisions in the middle layer (C3; Figure 3–figure
224 supplement 1E-G; Xiao et al., 2014; Schiessl et al., 2023 – pre-print). Cortical infection threads
225 appeared abnormally bulbous (Figure 3A and Figure 3–figure supplement 1E-F) and showed signs
226 of early abortion (Figure 3–figure supplement 1G; Laporte et al., 2014; Schiessl et al., 2023 – pre-
227 print). We observed that, even though the majority (76%) of crossed cortical cells were presumably
228 arrested in a GAP phase (low H3.1 content, n = 54; Figure 3–figure supplement 1F), such pausing
229 was not observed in about 24% of the inspected events. Here, infection threads were either blocked
230 or delayed in the outer cortex and the replicative H3.1 variant was retained (Figure 3A and Figure 3–
231 figure supplement 1G). Although the last infected cortical cells showed a significant nuclear
232 enlargement in all three genetic backgrounds investigated (Figure 3B), failure to coordinate

233 organogenesis and infection programs in the mutants resulted in an increased occurrence of infected
234 cells accumulating more H3.1 than their direct neighbours (Figure 3C). Together, these data reveal
235 that an appropriate reduction in cell-cycle activity and associated chromatin changes in infected cells
236 coincide with an efficient progression of cortical infection threads.
237
238 ***Cortical cells supporting transcellular infection control their commitment to cell division***
239 In Medicago and other plants producing indeterminate nodules, a local control of mitotic activity
240 could be especially important for rhizobia to timely cross the middle cortex, where sustained cellular
241 proliferation gives rise to the nodule meristem (Xiao et al., 2014). To investigate in greater detail
242 whether cells competent for transcellular infection are selectively kept away from transiting to
243 mitosis, we first used a triple fluorescent sensor enabling to track all cell-cycle phases *in planta*.
244 Originally developed for Arabidopsis, the plant cell-cycle indicator (PlaCCI) combines a component
245 of the pre-replication complex (CDT1a), the replicative histone variant (H3.1) and the N-terminal
246 domain of a B-type cyclin (N-CYCB1;1) as G1-, S- and late G2-phase reporters, respectively (Figure
247 4A; Desvoyes et al., 2020; Echevarria et al., 2021). The N-terminal domain of CYCB1;1 contains a
248 destruction box (D-box) ensuring a rapid turnover of the protein after one mitotic cell cycle. These
249 cell-cycle markers are expressed at early stages of organ development but disappear in terminally
250 differentiated cells (Desvoyes et al., 2020). When expressing the PlaCCI construct in transgenic
251 Medicago roots, all three markers were successfully visualized in reactivated cortical cells upon
252 nodule primordium formation (Figure 4B–C). Cortical cells passed by an infection thread kept low
253 but detectable amounts of the Arabidopsis H3.1 variant, indicating that they transited through S-phase
254 (Figure 4C). However, these cells stopped before accumulating substantial levels of N-CYCB1;1, in
255 contrast to their direct neighbours. We also confirmed latter observations when using an Arabidopsis
256 CYCB1;2-based fluorescent reporter (Figure 4D), labelling only cells that transit through G2/M
257 (Figure 4–figure supplement 1A; Weimer et al., 2016). Together, these results verified a selective
258 decrease in mitotic competence occurring on the cortical infection thread trajectory (Yang et al.,

259 1994) as rhizobia pass the middle cortical layer (C3) in Medicago roots. Importantly, we did not
260 observe the G1-phase marker accumulating in cells undergoing infection (Figure 4C), favouring the
261 hypothesis of a cell-cycle arrest and exit decision (Figure 2E) rather than a rapid switch to another
262 endoreduplication round (Desvoyes et al., 2019 – pre-print).

263 We next tested whether transcriptional reporters of a target gene necessary to execute cell
264 division get selectively repressed on the path of a cortical infection. The late G2/M gene *KNOLLE*
265 codes for a syntaxin protein specialized in angiosperm cytokinesis and is oppositely controlled when
266 cells do (Haga et al., 2007) or shall not (Takahashi et al., 2019) commit to mitosis. The transcription
267 of *KNOLLE* and other late cell-cycle genes (*e.g.*, *CYCB1;2*) in Arabidopsis is primarily regulated by
268 mitosis-specific activator (MSA) cis-elements present in their promoters that are targeted by
269 activator- and repressor-type three Myb repeats (MYB3R) transcription factors (Haga et al., 2007;
270 Kobayashi et al., 2015). Mutations in all three MSA core sequences present in the Medicago *KNOLLE*
271 promoter significantly reduced the expression of a β-glucuronidase (*GUS*) reporter gene in *Nicotiana*
272 *benthamiana* leaf cells in the presence of a hyperactive form of a MYB3R transcriptional activator
273 (NtmybA2Δ630; Figure 4–figure supplement 1B; Araki et al., 2004), suggesting that the Medicago
274 *KNOLLE* gene can be used as a *bona fide* late G2/M readout. Using the pKNOLLE::NLS-3xVenus
275 construct, we found that the activation of the *KNOLLE* promoter was lower on the cortical infection
276 thread trajectory in comparison to neighbouring, proliferating cells from nodule primordia (Figure
277 4E). An equivalent construct, ensuring the timely elimination of fluorescent reporters after one
278 canonical cell cycle (pKNOLLE::D-box-3xVenus-NLS; Figure 4–figure supplement 1C),
279 corroborated a selective control of the G2/M transition in cells undergoing transcellular infection.
280 Combining our observations of enlarged nuclei (Figure 2C), the absence of a G1 marker and the
281 reduced H3.1 levels and expression of mitotic genes (Figure 2D and Figure 4B–E), we conclude that
282 the initial cortical cells along the infection thread trajectory conduct a single cell-cycle round and stay
283 in a post-replicative (*i.e.*, G2) phase as long as they are crossed.

284 We further took advantage of the fact that the PlaCCI sensor provides a full view on cell-cycle
285 phase progression in root tissues, in Arabidopsis (Desvoyes et al., 2020) and Medicago (this study).
286 CDT1a- and CYCB1;1-associated signals in the root tip enabled us to identify 2C (*i.e.*, G1) and 4C
287 (*i.e.*, G2) nuclei, respectively (Figure 4-figure supplement 2A) – where 2C and 4C chromatin-values
288 correspond to the DNA content of a basic diploid genome. Measuring the area of nuclei exhibiting
289 the CYCB1;1-YFP signal in cortical layers of the root apical meristem (root tip) or the nodule
290 primordium revealed that they were on average 1.57 or 1.63 times larger than the ones producing
291 CDT1a-CFP, respectively (Figure 4-figure supplement 2B). This is in agreement with an increased
292 DNA content as cells transit from the G1- to the late G2-phase. Surprisingly, proliferating nodule
293 cells contained significantly wider nuclei than their diploid counterparts in the proliferation zone of
294 the root apical meristem (Figure 4-figure supplement 2B), suggesting a higher ploidy level early on.
295 These results lead to the intriguing possibility that reactivated inner cortical cells in Medicago enter
296 the mitotic cell cycle with an increased amount of genetic material.
297
298 ***Proliferation of endopolyploid cortical cells is a distinctive feature of Medicago root nodules***
299 Our data suggest that the dividing cortical cells contributing to nodule primordium formation are
300 polyploid – *i.e.*, that they contain more than the two genome copies of a diploid (2n) cell, where "n"
301 refers to the number of separate chromosomes. To assess this further, we identified and used the
302 centromere-specific histone H3 variant (CENH3) from Medicago as a marker of individual
303 chromosomes. Such fluorescently-tagged CENH3 proteins have already been successfully applied
304 for chromosome quantification *in planta* (Lermontova et al., 2006; De Storme et al., 2016). Aligning
305 the Medicago CENH3 amino acid sequence (G8A083) with characterized CENH3 sequences from
306 *L. japonicus*, Arabidopsis, *H. vulgare* and *Oryza sativa* revealed the presence of canonical CENH3
307 features (Figure 5–figure supplement 1), including a variable N-terminal tail and the centromere
308 targeting domain (CATD). When expressing a mCitrine-CENH3 fusion protein under the control of
309 its own promoter (pCENH3::mCitrine-CENH3), CENH3 labelled up to 16 nuclear foci and localized

310 exclusively at the presumed centromeres during mitosis (Figure 5A and B) in diploid root tip cells.
311 As the signal was rather weak, we scored centromeric foci in roots ectopically expressing the protein
312 (pUbi::mCitrine-CENH3; Figure 5A). Here, a reliable signal was observed in an increased proportion
313 of nuclei (82%) displaying not more than 14 to 16 mCitrine-CENH3 foci (versus only 55% when
314 *CENH3* was expressed under its endogenous promoter; n = 55; Figure 5B) – reflecting the base ploidy
315 in *M. truncatula* with 2n = 16. We therefore used the pUbi::mCitrine-CENH3 reporter construct for
316 our further analyses.

317 In a first set of experiments, we used CENH3 to discriminate between polyploid cells
318 undergoing endomitosis or endocycling. In endomitosis, entire chromosome replication and partial
319 mitotic progression result in a doubling of the chromosome / centromeric foci number (Iwata et al.,
320 2011; De Storme et al., 2016). By contrast, endocycling cells undergo repeated rounds of DNA
321 synthesis without segregating the newly replicated parts (Edgar et al., 2014). Here, copied
322 chromosome arms do not condense and spatial separation of sister kinetochores does not occur, so
323 that the number of compact CENH3 signals corresponds to the initial number of chromosomes (up to
324 8C; Figure 5–figure supplement 2A; Lermontova et al., 2006). As the occurrence of endocycling cells
325 has been previously reported in tissues infected by AM fungi, we first tested the CENH3-reporter in
326 roots inoculated with *Rhizophagus irregularis*. Indeed, cortical cells entered by the fungus displayed
327 large nuclei with no more than 16 labelled foci (Figure 5–figure supplement 2B), supporting their
328 endocycling nature (Carotenuto et al., 2019a; Lermontova et al., 2006). Up to 16 CENH3 foci were
329 also observed in diploid cortical cells from the root tip and pericycle cells from lateral root primordia
330 (Figure 5–figure supplement 2C). However, the majority of nodule cells exhibited between 26 and
331 32 fluorescent centromeric foci (75,5% in nodule primordia from stage IV to VI, n = 106; Figure 5–
332 figure supplement 2B–C) and a visibly increased number of chromosomes on mitotic figures (Figure
333 5–figure supplement 2B). These observations strongly support previously published data proposing
334 that proliferating cortical cells giving rise to Medicago root nodules are tetraploid (4n = 32; Torrey
335 & Barrios, 1969).

336 We next tested whether endopolyploid cells are already present at an earlier stage of nodule
337 development, where cell division events are confined to the pericycle, the inner cortical cells (C4,
338 C5) and occasionally occur in the third (C3) and second (C2) cortical layers (Figure 5C; Xiao et al.,
339 2014). Indeed, cells originating only from cortical cell divisions (C2 to C5) showed an increased
340 number of chromosomes (Figure 5D-E) compared to recently divided cells originating from the
341 pericycle (Figure 5E). Notably, cells performing anticlinal divisions in the middle cortex (Figure 5D,
342 left panel) that will later be crossed by the infection thread (Figure 5E, violet triangle) were also
343 polyploid. From these observations, we concluded that a key feature of cortical cells in Medicago
344 nodules is their ability to segregate a higher number of chromosome copies - corresponding to 8C in
345 a tetraploid cell entering mitosis.
346
347 ***Infected cells within the nodule primordium selectively halt their preparations for mitosis***
348 In a next set of experiments, we studied to which extent the cells positioned on the infection thread
349 trajectory (C3 to C4/5) prepare for mitosis. For this, we made use of the pre-mitotic loading
350 characteristics of CENH3 to the centromeres, which mainly occurs during the G2 phase and prior to
351 the spatial separation of sister kinetochores (Figure 6A; Lermontova et al., 2006, 2007, 2011). In
352 proliferating populations of the root tip (Figure 6–figure supplement 1A-B) and nodule primordia
353 (Figure 6A-B), late G2 cells contained large nuclei where the majority of sister kinetochores was split
354 and appeared as twin foci. We further noticed that centromere separation in Medicago is a gradual
355 rather than a simultaneous process, as root tip cells with comparable nuclear areas often exhibited an
356 intermediate number of fluorescent doublets (Figure 6–figure supplement 1A) of similar appearance
357 and length on a single focal plane (Figure 6–figure supplement 1B–D). To address the question to
358 which extent cortical cells that are competent for infection progress through the G2 phase and commit
359 to nuclear division, we assessed the gradual formation of sister centromeres. Although the nuclear
360 size of infected C3 cells suggested an 8C DNA content, as found in late G2-phase cells of the nodule
361 tissue (Figure 6B, C), none of these infected cells showed the typical CENH3 twin foci formed when

362 sister kinetochores split (n = 13; Figure 6B and D). Such control over mitotic commitment was tightly
363 maintained in the majority of infected, C4/5-derived cells (75,5%; n = 53; Figure 6D) which did not
364 display any visible sign of centromere separation across image stacks (Figure 6B), despite a
365 presumably duplicated genomic DNA content (Figure 6C). A smaller proportion of the recently
366 infected cells (20,7%) partially prepared for chromosome segregation and showed up to 3 fluorescent
367 doublets (Figure 6D) of comparable lengths to those measured in G2-phase progressing cells (Figure
368 6E), whereas only two cells (3,8%) with internalized bacteria got closer to nuclear and likely to cell
369 division (Figure 6B and D). Together, by combining several marker strategies based on histone H3
370 dynamics and on *bona fide* mitotic reporters, we conclude that most middle (C3) and inner (C4/5-
371 derived) cortical cells competent for intracellular infection enter a post-replicative, G2-type phase
372 without proceeding towards M-phase. Endopolyploid cortical cells hosting infection threads have
373 presumably gained the ability to execute a differentiation program rather than entering cell division
374 at the end of G2.
375
376 ***The symbiosis-specific NF-YA1 subunit holds potential to modulate the G2/M transition***
377 Our data suggest that cell-cycle progression and bacterial infection are highly coordinated, although
378 the precise molecular players able to redirect cell-cycle decisions while promoting cortical infections
379 remain to be identified. Prominent candidates are NF-YA1 proteins that were evolutionary recruited
380 to RNS, where they sustain both organogenesis and intracellular infection in a range of nodulating
381 legume and non-legume species (Combier et al., 2006; Laporte et al., 2014; Xiao et al., 2014; Hossain
382 et al., 2016; Bu et al., 2020). NF-YA1 plays an unambiguous role as a positive regulator of cell
383 divisions (Soyano et al., 2013) but was also recently shown to function in the early differentiation
384 and specification of nodule cells in Medicago (Schiessl et al., 2023 – pre-print). This prompted us to
385 assess whether NF-YA1 could act as a switch at mitotic entry. To test this, we used WT NF-YA1 and
386 a mutated variant lacking a functional DNA-binding domain (mutDBD) as eGFP fusion proteins. As
387 expected, both variants localized to the nucleus in *N. benthamiana* epidermal cells (Figure 7A;

388 Laporte et al., 2014). To foster cell cycle re-entry in such differentiated cells, we ectopically expressed
389 the Arabidopsis D-type cyclin *CYCD3;1* in mature leaves as described in the recently developed 'cell
390 division-enabled leaf system' (CDELS; Xu et al., 2020). As these re-activated cells commit to mitosis
391 and perform cytokinesis (Figure 7B), they also enable the activation of promoters containing MSA
392 cis-elements (Xu et al., 2020) as found in the Medicago *KNOLLE* promoter (Figure 4–figure
393 supplement 1B). We confirmed this by expressing eGFP-KNOLLE from its endogenous promoter in
394 the absence and presence of Arabidopsis CYCD3;1. The KNOLLE fusion protein was only detected
395 when co-expressed with CYCD3;1 using immunoblot analyses (Figure 7–figure supplement 1A) and
396 labelled newly formed cell-division planes (Figure 7–figure supplement 1B). This is consistent with
397 previous reports showing that the syntaxin KNOLLE accumulates only in dividing cells. We also
398 confirmed the activation of the Medicago *KNOLLE* promoter (pKNOLLE::GUS) in CDEL samples
399 ectopically expressing CYCD3;1 by using a fluorometric GUS assay (Figure 7C). Next, we tested the
400 impact of NF-YA1 on the activity of promoters driving cell cycle-dependent gene transcription in the
401 CDEL samples. While the presence of NF-YA1 did not alter *GUS* expression when driven from the
402 histone *H4* promoter (pH4::GUS) that is active during DNA synthesis (Figure 7C-D; Yang et al.,
403 1994), it significantly repressed pKNOLLE::GUS activation (Figure 7E). This effect was fully
404 abolished when using the mutated NF-YA1^{mutDBD} variant (Figure 7E). Interestingly, the repressive
405 effect of NF-YA1 was stronger compared to the one observed when using a MYB3R transcriptional
406 repressor from Medicago (Figure 7–figure supplement 2A–B) known to halt the expression of late
407 G2/M genes (Haga et al., 2007; Takahashi et al., 2019). These results suggest that the NF-YA1 DNA-
408 binding subunit prevents an unscheduled entry into mitosis in de-differentiating leaf cells, despite the
409 action of ectopically-expressed CYCD3;1.

410 We then tested whether such effect could be observed at the cellular level in the CDEL system.
411 For this, we ectopically co-expressed non-fluorescently-tagged CYCD3;1 and NF-YA1 and
412 additionally transformed these leaves with fluorescently tagged Medicago H3.3 and KNOLLE
413 proteins, expressed from their native regulators (Figure 7–figure supplement 1B). While the

414 constitutive presence of NF-YA1 did not prevent cell division events *per se*, a significantly lower
415 proportion of transformed cells produced detectable levels of KNOLLE (Figure 7–figure supplement
416 1C), indicating that less pavement cells engaged in mitosis at the investigated experimental timepoint.
417 Cells visibly accumulating the KNOLLE protein still progressed through M-phase in the presence of
418 NF-YA1 (Figure 7–figure supplement 1B), although a smaller proportion of them fully completed
419 cell division at 64 hours when compared to the control samples (Figure 7–figure supplement 1D).
420 From these data we concluded that NF-YA1 is able to control mitotic entry in de-differentiating,
421 endoreduplicated cells at least in the CDEL system. Since symbiotically infected middle and inner
422 primordium layers, where *NF-YA1* expression was found to be confined in (Laporte et al., 2014; Liu
423 et al., 2019b), are comprised of endopolyploid cells (Figure 5C–E), we hypothesize that the Medicago
424 NF-YA1 protein might similarly modulate cell-cycle progression during symbiotic infections of
425 legume roots by rhizobia.

426

427 **DISCUSSION**

428 Failure to timely coordinate infection and organogenesis programs in the root cortex results in the
429 formation of poorly colonized nodules that are unable to support the plant's demand to obtain fixed
430 nitrogen (Guan et al., 2013; Laporte et al., 2014; Schiessl et al., 2023–pre-print). Here, we sought to
431 understand at cellular resolution, whether cell-cycle progression and cellular reprogramming are
432 altered in a spatially confined array of host cells that gain a time-limited stage of competence for
433 transcellular infection.

434 Our data support a model where dividing cells contributing to nodule formation, including
435 target cells for cortical infection, are polyploid and contain 4 copies (C) of each chromosome (Figure
436 5D–E). In Medicago, these 4C cells either pre-exist in the root cortex (Vinardell et al., 2003;
437 Carotenuto et al., 2019a; Carotenuto et al., 2019b) or arise from a single endoreduplication round
438 prior to their possible entry into cell division (Libbenga & Torrey, 1973). As competent cells are
439 crossed by a cortical infection thread or fully internalize bacteria and despite being embedded into a

440 proliferating tissue, they reach an 8C DNA content (Figure 6C and Figure 8) but without committing
441 to a subsequent cell division (Figure 4C–E). Rather, cells supporting transcellular infections
442 presumably use a cell-cycle GAP phase after DNA replication (*i.e.,* G2) and extend such phase to
443 remodel their histone H3 composition (Figure 2A–B and D). Finally, this differentiation process and
444 concomitant transcellular passage are accomplished within a single, last cell-cycle round (Figure 2E;
445 Otero et al., 2016). Here, and similar to infected root hairs (Breakspear et al., 2014), a rapid switch
446 to another endocycle is likely prevented as both G1- and S-phase markers are kept low (Figure 4C).
447 Taken together, these events control a cell-cycle progression state where molecular players operate
448 to ensure a successful transmission of rhizobia to the first nodule cells.
449
450 **Modulating endopolyploidy during rhizobial infections**
451 In line with findings from Arabidopsis reporting that a downregulation of *H3.1* gene expression and
452 a massive eviction process contribute to various differentiation programs, *e.g.*, in the male and female
453 gametes (Ingouff et al., 2010), the root meristem, the embryo (Otero et al., 2016) and the female
454 germline precursor (Hernandez-Lagana & Autran, 2020), we show that the genetic program enabling
455 intracellular infections of Medicago roots accesses the same mechanism (Figure 2A–B and Figure 2–
456 figure supplement 1C–E). Reciprocally, our data indicate that high H3.1 levels tend to be maintained
457 in infected cells with blocked or aborted infections (Figure 3A and C and Figure 3–figure supplement
458 1A–D). Furthermore, the nuclear enlargement in infected cells (Figure 2C) indicates profound
459 transcriptional reprogramming and activation of new gene regulatory networks, as previously shown
460 to occur in LCO-treated (Knaack et al., 2022) or young symbiotic cells (*i.e.*, infected root hairs and
461 8C cells from mature nodules; Breakspear et al., 2014; Nagymihály et al., 2017; Liu et al., 2019a).
462 We expanded the latter view by showing that tetraploid cortical cells passed by an infection thread
463 also reach a presumable 8C DNA content (Figure 6C). As reported for growing cell types in
464 Arabidopsis (Bhosale et al., 2018), such alteration in endopolyploidy might support, among others,
465 changes in cell wall composition, which have also recently been demonstrated to occur specifically

466 around infected cells in Medicago (Su et al., 2023; Gaudioso-Pedraza et al., 2018). In the determinate
467 nodulator *L. japonicus*, polyploidization of early nodule cells might be controlled by *VAGRANT*
468 *INFECTION THREAD 1* (*VAG1*), a putative component of the DNA topoisomerase VI (topo VI)
469 complex, as cortical cells with reduced ploidy levels cannot be infected in the *vag1* mutant (Suzaki
470 et al., 2014).

471 Interestingly, but different to infections by mycorrhizal fungi where repetitive rounds of
472 endoreduplication occur (Russo & Genre, 2021) and support fungal colonization (Figure 1C;
473 Carotenuto et al., 2019a; Carotenuto et al., 2019b), markedly reduced histone H3.1 contents in cells
474 maintaining rhizobial infections in the root cortex up to the first recipient cells in nodule primordia
475 indicate reduced endocycling rates (Figure 2D-E; Otero et al., 2016). Such attenuation of cell-cycle
476 progression together with decreased transcript levels of mitotic cyclins were shown to occur in
477 budding yeast and Arabidopsis (Negishi et al., 2016; Gigli-Bisceglia et al., 2018) following the
478 activation of a cell-wall integrity (CWI) checkpoint. More recently, Ma and colleagues proposed a
479 scenario where the CWI kinase THESEUS1 (THE1), with a related gene being induced in infected
480 root hairs (Breakspear et al., 2014; Liu et al., 2019a), triggers cell wall stiffening as a response to
481 endoreduplication attenuation (Ma et al., 2022).

482

483 **A G2-phase arrest and attenuated endoreduplication as a plausible context for cortical**
484 **infections**

485 Reaching and staying in a pre-mitotic stage has been proposed to facilitate the long-distance
486 progression of infection threads in legume species forming so-called cortical, pre-infection threads
487 (PITs) (Yang et al., 1994; Timmers et al., 1999; Foucher & Kondorosi, 2000). These structures
488 resemble the onset of a cell division plane that requires the formation of a cortical division zone,
489 which is established from late S- through G2 phases (Costa, 2017). Interestingly, this cell-cycle
490 progression window coincides with the one we observed in infected cortical cells (Figure 2A–E and
491 Figure 4A–C). In addition, the existence of pre-mitotic and G2-arrested cortical cells on the infection

492 thread trajectory is in line with a recent report showing that a rhizobium-induced mitotic module,
493 comprising an α-Aurora kinase gene and its MYB3R transcriptional activator, supports
494 endosymbiotic infection in Medicago (Gao et al., 2022). Interestingly though, overexpression of the
495 activator-type *MYB3R1* gene resulted in the formation of abnormally bulbous or branched infection
496 threads (Gao et al., 2022). These data emphasize the need to balance the activity of transcriptional
497 regulators driving mitosis and cytokinesis in infected cells.

498 In summary, we hypothesize that endocycle suppression after a round of DNA replication
499 (Breakspear et al., 2014) and exiting the cell-cycle from the G2-phase might therefore create a
500 permissive, yet controlled state for cortical infection thread progression, where polarization and cell-
501 wall remodelling factors specialized for intracellular infection (Lace et al., 2023; Su et al., 2023) act
502 in a defined cell-cycle window to sustain infection thread growth and guidance across cortical layers.
503

504 **Endopolyploidization following cytokinin perception: a legume innovation?**

505 Using the centromeric histone H3 (CENH3) fluorescent reporter enabled us to assess the number of
506 chromosomes, the progression through the G2 phase (Figure 6–figure supplement 1A–B; Lermontova
507 et al., 2006) and to clearly identify diploid and polyploid cells (Figure 5 B and E; De Storme et al.,
508 2016). Combining CENH3 patterns with the histone H3.3 marker showed that somatic cortical cells
509 giving rise to indeterminate Medicago root nodules are mainly tetraploid, which is consistent with
510 previous observations (Torrey & Barrios, 1969). Furthermore, our imaging data indicate that dividing
511 endopolyploid cells are homogenously maintained in the nodule tissue (Figure 5–figure supplement
512 2B–C). This suggests that tetraploidization is an important feature for nodule fitness and infectability,
513 as it may enable processes such as the required integration of many contextual stimuli (*e.g.,* bacterial
514 signals; Russo & Genre, 2021), the coordination of controlled organogenesis and a greater cellular
515 adaptability to hypoxic environments as also suggested for human tumour cells (Yant & Bomblies,
516 2015). Furthermore, our findings point towards tetraploidization of cortical cells being a hallmark for
517 nodule identity as pericycle cells in nodule or lateral root primordia remain strictly diploid (Figure

518 5E and Figure 5–figure supplement 2C). Interestingly, when dissected and cultured in suspension,
519 cortical cells from the susceptible zone of pea roots entered cell divisions as tetraploid cells only
520 when cytokinin (kinetin) was applied in addition to auxin (2,4-D; Libbenga & Torrey, 1973). This is
521 particularly interesting since a specific cortical response to cytokinin, an auxin/cytokinin interplay
522 and subsequent cellular proliferation in the root cortex appear to be a legume innovation (Guan et al.,
523 2013; Gauthier-Coles et al., 2019).
524
525 **NF-YA1, possible intermediary between intracellular infection and cell-cycle control**
526 While this and other reports have shed light onto cell-cycle patterns during rhizobial infections in
527 roots and nodules, genetic factors coordinating cell-cycle progression and intracellular infections
528 remained enigmatic. Using the heterologous CDEL system (Xu et al., 2020) has enabled us to test the
529 impact of at least one of the potential candidates, the symbiotic transcription factor NF-YA1, on cell
530 cycle-dependent activities in a de-differentiating cellular population. Expression of NF-YA1 in this
531 system did not prevent cells from passing through S-phase (Figure 7D). But, while the activated cells
532 (as indicated by the induction of the KNOLLE reporter) still engage in mitosis and eventually divide
533 (Figure 7–figure supplement 1B), significantly fewer transformed cells promoted the expression of
534 this G2/M marker at our experimental timepoints (Figure 7E and Figure 7–figure supplement 1C)
535 These results strongly suggest that, in the CDEL system, NF-YA1 negatively regulates the entry into
536 mitosis despite the presence of CYCD3;1. The latter has been shown to promote mitotic cycles and
537 to restrain differentiation and endoreduplication when accumulated in shoot tissues (Schnittger et al.,
538 2002; Dewitte et al., 2003). Our observations are also consistent with findings in mammalian cells,
539 where the NF-Y trimer mediates the repression of key mitotic genes in complex with the WT p53
540 protein (Imbriano et al., 2005) during a G2 arrest induced by genotoxic stress (Manni et al., 2001). A
541 link to DNA damage control, potentially arising when endoreduplicated pavement cells are pushed
542 back into a chromosome segregation cycle, seems likely in the CDEL system. However, whether NF-
543 YA1 similarly monitors cell division activity in polyploid nodule primordium cells (Figure 5E) and

544 controls the G2/M transition along the infection thread trajectory and in intracellularly colonized
545 nodules (Figure 6B) are aspects that need to be addressed independently.
546
547 In summary, we propose that a local control of cell-cycle activity and a cell-cycle exit decision along
548 the infection thread trajectory provide a window of cellular competence for cortical infections to
549 progress down to the nodule primordium niche in Medicago. We demonstrated that the cell division
550 and differentiation potentials are controlled in a spatially confined cell-file in the root cortex. We also
551 showed that post-replicative, tetraploid cells reaching an 8C DNA content are optimal for intracellular
552 infection. Consequently, it is tempting to hypothesize that exactly these cells comprise a highly
553 specific transcriptional and regulatory landscape that ultimately defines the molecular susceptibility
554 state for intracellular infection competence.
555
556
557 **MATERIALS AND METHODS**
558 **Plant materials and growth conditions**
559 The *Medicago truncatula* (Medicago) wild-type (WT) ecotype A17, cultivar Jemalong was used in
560 this study. The *daphne-like* (FN8113) and *nf-ya1-1*mutant lines have been described previously (Liu
561 et al., 2019b; Laporte et al., 2014). Seeds from the *daphne-like* mutant were kindly provided by Rene
562 Geurts (Laboratory of Molecular Biology, Wageningen University, The Netherlands).
563 Seeds were scarified by covering them with sulfuric acid (H_2SO_4) 96% for 8 minutes and washed 6
564 times with sterile tap water. After surface sterilization with a bleach solution (1.2% sodium
565 hypochlorite, NaClO and 0.1% sodium dodecyl sulfate, SDS) for 1 min, the 6 washing steps were
566 repeated and seeds were sown on 1% (w/v) agar plates. Seeds were then stratified at 4 °C for 5 days
567 in the dark before being germinated at 22 °C in the dark for 16 h.
568
569

570 **Hairy root transformation**

571 Composite Medicago plants were generated with transgenic hairy roots as previously described
572 (Boisson-Dernier et al., 2001). *Agrobacterium rhizogenes* ARquaI cells carrying the desired binary
573 vector were cultured in liquid LB medium containing appropriate antibiotics at 28 °C, shaking
574 overnight. Three hundred µl of the culture (OD 600 nm: 0.5-0.7) were plated on solid LB medium
575 with corresponding antibiotics and incubated at 28 °C for 2 days. Plants were prepared by removing
576 the seed coat from germinated seedlings and about 5 mm of the root tip region was removed before
577 the cut site was dipped into the solid *A. rhizogenes* culture. Up to 25 inoculated seedlings were placed
578 on solid Fahräeus medium supplemented with 0.5 mM NH_4NO_3. Transformed seedlings were then
579 grown vertically in a climate chamber at 21° C for 3 days in the dark. After another 4 days at 21 °C
580 (16 h light/8 h dark, 35 µmol m^{-2} s^{-1} light intensity), with only the roots protected from illumination,
581 composite plants were transferred to fresh solid Fahräeus plates (0.5 mM NH_4NO_3) and grown for 10
582 days at 22 °C following the same photoperiod. Transgenic roots were visualized based on the
583 fluorescence emitted by nuclear markers (*M.t.* pH3.3::H3.3-mCherry; *A.t.* pH3.1::H3.1-mCherry;
584 pLjUbi::NLS-2xmCherry) using an AXIO Zoom.V16 stereomicroscope (Zeiss). Un-transformed
585 roots were removed and the composite plants were transferred in pots (7x7x8 cm) containing a 1:1
586 (v/v) mixture of quartz sand (0.1–0.5 mm grain size, Sakret) and vermiculite (0–3 mm, Ökohum)
587 equilibrated with 25 ml of a ¼ Hoagland solution (0.1 mM KNH3). After 4 days of acclimation (16/8
588 h light/dark photoperiod, 24 °C temperature, 60% humidity and 70-90 µmol m-2 s-1 light intensity),
589 plants were subjected to rhizobial inoculation.

590 For this, *Sinorhizobium meliloti* (Sm2011) strains producing mCherry or GFP were grown on solid
591 TY medium containing 10 µg/ml tetracycline for 2 days at 28 °C. A single colony was used as an
592 inoculum and bacteria were grown in liquid TY medium containing the antibiotic at 28 °C, shaking
593 for 2 days. Cells were centrifuged for 8 min at 2205 g, washed once with liquid Fahräeus medium
594 and finally resuspended into the same medium to reach an OD 600 nm of 0.0015. Five ml of this
595 bacterial suspension were applied to each composite plant. Pots were watered twice a week with tap

596 water and fertilized with a ¼ Hoagland solution (0.1mM KNO_3) once a week. Transgenic roots were
597 harvested at different timepoints (8 to 14 days) for tissue fixation, clearing and deep tissue imaging
598 by confocal microscopy.
599
600 **Construct design**
601 For expressing the canonical (*H3.1*) and replacement (*H3.3*) histone genes of Medicago, genomic
602 fragments containing the promoters (*H3.1*: 2623 bp; *H3.1* (2): 2580 bp; *H3.3*: 2739 bp) and open
603 reading frames (ORF) except the termination codon were used. The pH4::GUS reporter used in
604 quantitative fluorometric assays comprised a 2080 bp fragment of the promoter. Expression of the
605 centromeric histone (*CENH3*) gene (coding sequence) was driven by a tentative promoter comprising
606 1000 bp upstream of the start codon. Transcriptional KNOLLE reporters were driven by a 2325 bp-
607 long fragment of the *KNOLLE* promoter. The core pentamer of all three mitosis-specific activator
608 (MSA) cis-elements (AACGG) within the *KNOLLE* promoter was mutated by changing two bases
609 (ATTGG) according to Ito et al., 2001. The *KNOLLE* genomic sequence was used to build the
610 translational reporter (pKNOLLE::eGFP-KNOLLE). For Medicago NF-YA1, the genomic sequence
611 was used and the NF-YA1^{mutDBD} variant was created by replacing the conserved RGC amino acid
612 residues (positions 213-215) by an AAA triplet according to Laloum et al., 2014. For the repressor-
613 type *MYB3R* transcription factor, the coding sequence (CDS) was used. All Medicago sequence
614 information was obtained from the Mt4.0v1 genome through Phytozome.
615 The *Arabidopsis thaliana* (Arabidopsis) pCYCB1;2::N-CYCB1;2-NLS-3xVenus reporter construct
616 was designed according to Trolet et al., 2019 and included a genomic fragment (AT5G06150) of 1929
617 bp, comprising 1090 bp of promoter sequence, the 5' untranslated region and 839 bp from the ORF
618 including the first intron. Addition of 2 bases (GG for Gly) at the 3' end of this genomic fragment
619 enabled the production of the N-terminal CYCB1;2 domain (including the destruction box [D-box]
620 motif) fused in-frame to a triple-Venus nuclear reporter (Binder et al., 2014; Nadzieja et al., 2019).
621 The CYCB1;1 N-terminal (D-box) domain was produced from a genomic fragment (AT4G37490) of

622 713 bp including the first 2 introns (nucleotides [nts] 41-308 and 488-584) and 129 bp of the third
623 exon (nts 585-713). This module was fused in-frame to a triple-Venus nuclear FP to generate a
624 destabilized version of the fluorescent reporter. The CYCD3;1 (AT4G34160) CDS was placed under
625 control of the cauliflower mosaic virus (CaMV) 35S promoter (426 bp) and fused in frame to a 3xHA
626 module to build the p35S::CYCD3;1-HA construct. Arabidopsis sequence data can be found on
627 Phytozome (*Arabidopsis thaliana* TAIR10 annotation version). To produce the C-terminally
628 truncated, hyperactive version of the *Nicotiana tabacum* MybA2 transcriptional activator
629 (pLjUbi::eGFP-NtMybA2Δ630), the CDS (GenBank accession: AB056123.1) coding for the first
630 630 amino acid residues was used (Araki et al., 2004). The GoldenBraid PlaCCI transformation
631 plasmid was kindly provided by Bénédicte Desvoyes and Crisanto Gutierrez (Centro de Biologia
632 Molecular Severo Ochoa, CSIC-UAM, Madrid, Spain).

633 **Construct production using the Golden Gate cloning system**

634 The Golden Gate modular cloning (MoClo) system was used to generate binary plasmids for
635 transgene expression in plant cells (Weber et al., 2011). Promoter, genomic and coding sequences
636 were synthetized and cloned into pMS-RQ (GeneArt, Thermo Fisher Scientific, Regensburg,
637 Germany). Level 0 (L0) functional modules used in this study are held for distribution in the ENSA
638 project collection (https://www.ensa.ac.uk/). Details of the L1 expression cassettes and L2 binary
639 vector composition, including used promoters, genetically encoded fluorescent proteins (stable or
640 short-lived) or epitope tags and the accession numbers for requesting constructs, are provided in a
641 supplementary file (Table S1). One-pot reactions using the Type IIS restriction enzymes BsaI-HFv2
642 (R3733S) and BpiI / BbsI-HF (R3539S) and the T4 DNA ligase (M0202S), all from New England
643 BioLabs (Frankfurt am Main, Germany), were assembled according to Binder et al., 2014. Cut-
644 ligation reactions were cycled 50 times between 37 °C for 2 min and 25 °C for 5 min, followed by 5
645 min at 50 °C and 5 min at 80 °C. Five µl of the reaction were transformed into *Escherichia coli* Stbl3
646 (for L1 and L2 plasmids carrying histone H3.1 or H3.3 expression cassettes) or TOP10.

647 **Root colonization by *Rhizophagus irregularis***

648 Following excision of un-transformed roots, composite Medicago plants were transferred to chive
649 (*Allium schoenoprasum*) nurse pot (9 x 9 cm) systems containing *R. irregularis* (DAOM 197198,
650 sterile spore inoculum from Agronutrition, France) set up according to Demchenko et al., 2004 (4
651 plants x pot). Each pot was covered with a transparent plastic bag (20 x 30 cm) for two days to keep
652 plants in moisturized conditions. Plants were grown in a controlled environment chamber at 24 °C
653 with a 16/8 hour light/dark photoperiod, with each pot being watered every second or third day with
654 50 ml deionized water and fertilized once per week with 50 ml ¼ Hoagland medium. After 7 to 15
655 days of co-culturing, composite plants were harvested and excised transgenic roots were subjected to
656 fixation, clearing and Calcofluor White staining prior to imaging.

657

658 **Clearing and staining of the root material**

659 The presence of all expected fluorescent reporters was verified in the meristematic region using an
660 AXIO Zoom.V16 stereomicroscope (Zeiss) before further analyzing the transgenic roots. Fixation,
661 clearing and cell-wall counter-staining procedures were performed according to Ursache et al., 2018.
662 Briefly, transformed roots were isolated and fixed in a freshly prepared 4% paraformaldehyde (PFA)
663 solution in 1x phosphate-buffered saline (PBS), infiltrated under vacuum for 15 min and then gently
664 agitated for 60-120 min at room temperature in the dark. After 2 washes in 1x PBS, roots were
665 transferred to the clearing (ClearSee) solution and incubated 7 to 10 days with gentle shaking,
666 changing the ClearSee solution every 2 days. Prior to imaging, roots were stained with 0.1%
667 Calcofluor White in ClearSee for 1 h, before being rinsed once and washed in the clearing solution
668 for 30 min. Calcofluor White was imaged using a 405 nm laser diode excitation source and a 425–
669 475 nm detection window.

670

671

672

673 **Nodule sections**

674 To assess the localization pattern of H3.1 and H3.3 histone variants across different nodule zones,
675 composite plants were generated by hairy root transformation as described above. Nodules were
676 harvested 35 to 40 days after inoculation in open pots and fixed in 4% (w/v) PFA in 1x PBS, under
677 vacuum treatment for 15 min and then gently agitated for 45 min at room temperature. The fixed
678 samples were embedded in 6% (w/v) low melting temperature agarose (Biozym) and longitudinal
679 sections (70 µm thickness) were obtained using a VT1000S vibratome microtome (Leica Biosystems,
680 Mannheim, Germany).

681

682 **Fluorescent reporter imaging by Confocal Laser-Scanning Microscopy (CLSM)**

683 Imaging of plant material (*i.e.,* nodule semi-thin sections and cleared root samples) was performed
684 using a TCS SP8 confocal microscope (Leica Microsystems, Mannheim, Germany) controlled by the
685 LAS X v3 software. Images were acquired with a 20x/0.75 or a 40x/1.10 (HC PL APO CS2) water
686 immersion objective. Genetically encoded FPs were excited with an argon laser or a White Light
687 Laser (WLL) source. Emitted photons were collected using hybrid detectors (HyDs). eCFP was
688 excited with an argon laser line at 458 nm and the emission was detected at 470-510 nm. All other
689 FPs were excited with WLL excitation (ex) lines and emissions (em) were detected according to the
690 following settings: eGFP = 488 nm (ex) / 500-550 nm (em); YFP = 515 nm (ex) / 525-586 nm (em);
691 mCitrine and Venus = 515 nm (ex) / 525-550 (em); mCherry: 561 or 587 nm (ex) / 600-650 or 620-
692 650 nm (em).

693

694 **Image analysis and quantification of nuclear fluorescent signals**

695 All images were processed and analyzed using the Fiji/ImageJ open-source software (Schindelin et
696 al., 2012). Image files were used to create figure panels through the FigureJ plugin (Mutterer & Zinck,
697 2013). If not indicated differently, 2D maximum intensity projections of z-stacks are presented in the
698 figures. All quantitative measurements were performed on single focal planes and single channels

699 from un-processed z-stacks, acquired from fully transformed Medicago roots. The Fire lookup table
700 (LUT) was applied to facilitate the visualization of low-intensity pixels. Nuclear areas were measured
701 at the equatorial plane using the freehand selection tool, on channels displaying the signal from
702 chromatin-associated proteins (*i.e.*, H3.1 or H3.3-FP fusions). H3.1-eGFP levels were quantified in
703 the nucleus of infected cells (IC) and of directly adjacent, neighbouring cells (NC) present on the
704 same z-stack in the same cortical layer. For this, an outline was manually drawn around each nucleus
705 at the equatorial plane and area, integrated density and mean gray values were measured. Three oval
706 selections were drawn adjacent to all measured nuclei to be used for normalization against
707 background fluorescence. The corrected total nuclear fluorescence (CTNF) = integrated density –
708 (area of selected nucleus × mean fluorescence of background readings) was calculated according to
709 McCloy et al., 2014 using Excel. The number of mCitrine-CENH3 signals in individual nuclei and
710 mitotic figures was manually determined across image stacks using the multi-point tool. The length
711 of CENH3 fluorescent doublets was measured between the 2 most distant pixels using the straight-
712 line tool.
713
714 **Transient expression in *Nicotiana benthamiana* leaves**
715 Four to 5-week-old tobacco (*N. benthamiana*) plants were transiently transformed with *A. rhizogenes*
716 (ARqua1) cells carrying the construct of interest. The first, second and third fully expanded true
717 leaves were used for infiltration experiments using needle-less syringes. Agrobacteria were
718 resuspended in a MES/KOH infiltration buffer (10 mM, pH 5.6) supplemented with 10 mM $MgCl_2$
719 and 150 µM acetosyringone. Bacterial cultures used for co-transformations were diluted to a final OD
720 600 nm of 0.1 for each construct. *Agrobacterium tumefaciens* (GV3101) cells producing the p19
721 silencing suppressor (Silhavy et al., 2002), were systematically included at a final OD 600 nm of
722 0.05. Upon infiltration, plants were further grown for 64 to 72 h before harvesting leaf samples with
723 a biopsy puncher (4 mm diameter) in the distal half of fully infiltrated leaves. Four to 5 leaf discs

724 were either mounted in sterile tap water and imaged with a confocal microscope, or 10 leaf discs were
725 frozen in liquid nitrogen prior to *in vitro* transactivation assays.
726
727 **Cell division-enabled leaf system (CDELS)**
728 To foster differentiated pavement cells to enter the cell division cycle, non-fluorescently-tagged
729 Arabidopsis CYCD3;1 was expressed under control of the CaMV 35S promoter by Agrobacterium
730 infiltration (Xu et al., 2020). The p35S::CYCD3;1-HA construct was co-transformed with binary
731 vectors allowing native expression of cell cycle regulated-reporters (pH4::GUS, pKNOLLE::GUS,
732 pKNOLLE::eGFP-KNOLLE) and constitutive expression of transcription factors (NF-YA1, NF-
733 YA1^{mutDBD}) from Medicago. All plasmids used in the experiments involving the CDEL system are
734 listed in Table S1. Transformed leaves homogenously expressing nuclear transformation markers
735 included on the corresponding binary vectors were selected using an AXIO Imager.M2m ApoTome.2
736 light microscope (Zeiss). The activity of HA-tagged CYCD3;1 was verified by the presence of at
737 least one mitotic figure with chromosomes labeled by H3.3-mCherry before harvesting.
738
739 **Immunoblot analyses**
740 To detect proteins transiently produced in the CDEL samples, 3 discs from 64 h post-infiltration
741 leaves were frozen in liquid nitrogen and ground to powder using a Tissue Lyser MM300 (Retsch).
742 The powder was resuspended in 120 µl of 2x loading buffer and heated for 8 min at 95 °C. Equal
743 volumes of samples were loaded and separated by 10% SDS-polyacrylamide gel electrophoresis
744 (PAGE) at constant voltage (80V). Proteins were transferred to a PVDF membrane (0.2 µm pore size)
745 using the Trans-Blot® Turbo™ semi-dry transfer system (7 min mixed MW MIDI program) (Bio-
746 Rad). After blocking in a 2.5% (w/v) milk/TBST solution for 1 h at RT, transferred membranes were
747 hybridized overnight at 4 °C with the following primary antibodies: anti-GFP (Takara Bio Cat#
748 632381, RRID:AB_2313808) (1/5000); anti-DsRed (Takara Bio Cat# 632496, RRID:AB_10013483)
749 (1/5000); peroxidase-conjugated anti-HA (Roche Cat# 12013819001, RRID:AB_390917) (1/2000);

750 anti-FLAG M2 (Sigma-Aldrich Cat# F3165, RRID:AB_259529) (1/2000). Membranes were washed
751 and incubated 1 h at RT with peroxidase-conjugated secondary antibodies (anti-mouse, Sigma-
752 Aldrich Cat# A4416, RRID:AB_258167; anti-rabbit, Sigma-Aldrich Cat# A6154,
753 RRID:AB_258284) (1/2000). Immunoblotted proteins were detected using the Clarity Western ECL
754 Substrate (Bio-Rad). Digital images were acquired using an ECL ChemoCam Imager (Intas Science
755 imaging) with exposures stopped before saturation.
756
757 **Transactivation and quantitative fluorometric GUS assays**
758 *N. benthamiana* leaf samples used for GUS fluorometric assays were harvested 72 h post-infiltration.
759 The same number of plasmids was used for all co-transformation experiments. A construct driving
760 the accumulation of a nuclear FP (proH3.1::NLS:3xVenus) was included in the absence of exogenous
761 transcription factors. Ten leaf discs per transformed leaf were frozen in liquid nitrogen inside a Safe
762 Seal Micro tube containing a stainless-steel bead (5 mm diameter). Samples were ground twice for
763 30 s (28/s frequency) using a Tissue Lyser MM300 (Retsch) and the powder was resuspended in 400
764 µl of cold GUS extraction buffer (50 mM $NaHPO_4$, pH 7.0, 1 mM EDTA, 10 mM DTT, 0.05% [v/v]
765 Triton X-100 and 1x Protease Inhibitor Cocktail [Roche]). Crude leaf extracts were incubated for 2 h
766 at 4 °C on a turning wheel and centrifuged at 16.900 g for 5 min at 4 °C. Ten µl of the supernatant
767 were used to determine protein concentrations by the dye-binding Bradford assay (Bio-Rad). Twenty-
768 five µg of total proteins in a final volume of 100 µl were pipetted into a white 96 well plate (Greiner
769 Bio-One) before the addition of 200 µl of GUS reaction buffer (50 mM $NaHPO_4$, pH 7.0, 1 mM
770 EDTA, 1% [v/v] Triton X-100 and 0.5 mM 4-Methylumbelliferyl-β-D-glucuronide [4-MUG] [Carl
771 Roth]). After 10 min of incubation at 37 °C in the dark, the fluorescence emitted by GUS-mediated
772 hydrolysis of 4-MUG into 4-Methylumbelliferone (4-MU) was measured using a microplate reader
773 (POLARstar Omega, BMG LABTECH). Fluorescence was recorded at 360 nm excitation and 460
774 nm emission filter (gain 500, 20 flashes per well) every 5 min over a time period of 130–180 min.
775 Samples were run in technical triplicates and blank measurements (100 µl extraction buffer + 200 µl

776 reaction buffer) were performed to correct for any nonenzymatic hydrolysis of 4-MUG. Corrected
777 GUS activities (4-MU fluorescence units [FU] min^{-1}) were calculated as: $A_{GUS} = \Delta F / \Delta t = (F1-F0) /$
778 Δt where ΔF is the difference in fluorescence intensities measured in the linear range of the
779 fluorescence curves over a 15 min period of time (Δt). Values were normalized to 1 µg of protein
780 content by using the protein concentration determined via Bradford assay. Two to 5 independent
781 experiments were performed with at least 3 leaves from 2 different plants analyzed.
782
783 **Data visualization and statistical analysis**
784 Alignment of multiple protein sequences was performed using Jalview (version 2.11.2.6) (Procter et
785 al., 2021). Statistical analyses and generation of figures were performed using the GraphPad Prism
786 software (version 9.5.1) (GraphPad Software Inc.). Normal distribution of data was tested using the
787 Shapiro-Wilk and Kolmogorov-Smirnov normality tests. A Brown-Forsythe and Welch ANOVA test
788 followed by Dunnett's multiple T3 comparisons or an unpaired t-test with Welch's correction were
789 applied as parametric tests. Kruskal-Wallis followed by Dunn's multiple comparisons or Mann-
790 Whitney tests were applied as non-parametric tests. Boxes in the box-and-whiskers plots extend from
791 the 25th to 75th percentiles and whiskers range from the smallest to the largest values. Middle
792 horizontal lines are plotted at the median. Sample size n, statistical tests and significance levels are
793 provided in the figure legends. Source data and results of the statistical analyses are provided as
794 supplement files associated to the corresponding figure.
795
796 ***M. truncatula* gene identifiers**
797 Accession numbers for the Medicago genes used in this study are provided from the following
798 genome portals, Phytozome (Mt4.0v1 version; https://phytozome-next.jgi.doe.gov/) and / Medicago
799 truncatula A17 r5.0 (A17 r5.1.9 version; https://medicago.toulouse.inra.fr/MtrunA17r5.0-ANR/),
800 respectively: *H3.1* (1) (Medtr8g092720 / MtrunA17_Chr8g0383781); *H3.1* (2) (Medtr8g103245 /
801 MtrunA17_Chr8g0390361); *H3.3* (Medtr4g097175 / MtrunA17_Chr4g0054161); *H4*

802 (Medtr7g099610 / MtrunA17_Chr7g0262791); *KNOLLE* (Medtr5g012010 /
803 MtrunA17_Chr5g0398891); *CENH3* (Medtr8g027840 / MtrunA17_Chr8g0347231); repressor-type
804 *MYB3R* (Medtr7g061330 / MtrunA17_Chr7g0238631); *NF-YA1* (Medtr1g056530 /
805 MtrunA17_Chr1g0177091).
806

807 **DATA AVAILABILITY STATEMENT**

808 All data generated and analyzed during this study are included in the manuscript and supporting files.
809 All sequences have been obtained from publicly available repositories and indicated in the Materials
810 and Methods section.
811

812 **MATERIALS AVAILABILITY STATEMENT**

813 All material generated within this study can be obtained from the corresponding authors upon request.
814 Plasmids obtained from other laboratories as indicated in the respective sections need to be requested
815 from the original producer.
816

817 **ACKNOWLEDGEMENTS**

818 We would like to thank the entire team for the constant and fruitful input into the project and
819 especially Eija Schulze and Carmen Schubert for their excellent experimental support. Furthermore,
820 we greatly appreciated the technical help of Zenglin Li and Philipp Schwenk (University of Freiburg,
821 Germany) on GUS fluorometric assays. Jean Keller (LRSV Toulouse, France now Max-Planck
822 Institute for Chemical Ecology, Jena, Germany) conducted a comprehensive phylogeny on MYB3R,
823 MEME and FIMO searches on MSA motifs. Katharina Schiessl (University of Cambridge, UK)
824 provided the *nf-ya1-1* seeds and fruitful comments throughout the project. We also thank the staff of
825 the Life Imaging Center (LIC) in the Hilde Mangold House (HMH) of the Albert-Ludwigs-University
826 of Freiburg for the help with their confocal microscopy resources, and the excellent support in image

recording. The microscopes are operated by the Microscopy and Image Analysis Platform (MIAP) and the Life Imaging Center (LIC), Freiburg.

FUNDING

Engineering Nitrogen Symbiosis for Africa (ENSA) project currently supported through a grant to the University of Cambridge by the Bill & Melinda Gates Foundation (OPP1172165) and UK government's Department for International Development (DFID) (TO)

Deutsche Forschungsgemeinschaft (DFG, German Research Foundation) 431626755 (TO)

DFG under Germany's Excellence Strategy grant CIBSS – EXC-2189 – Project ID 39093984 (TL, TO)

China Scholarship Council (CSC) grant 201708080016 (CS)

DFG project number 414136422 (CLSM; TO)

AUTHOR CONTRIBUTIONS

Conceptualization: MB, TL, TO; Investigation: MB, BL, NZ, CS, SE, PK, JS, FAD; Writing – Original Draft: MB, TO; Writing –Review & Editing: MB, BL, NZ, CS, SE, PK, JS, FAD, TL, TO; Supervision: MB, TL, TO; Project administration: TO; Funding Acquisition: TL, TO

REFERENCES

Araki, S., Ito, M., Soyano, T., Nishihama, R., & Machida, Y. (2004). Mitotic cyclins stimulate the activity of c-Myb-like factors for transactivation of G2/M phase-specific genes in tobacco. *J Biol Chem*, *279*(31), 32979-32988. https://doi.org/10.1074/jbc.M403171200

Berckmans, B., & De Veylder, L. (2009). Transcriptional control of the cell cycle. *Curr Opin Plant Biol*, *12*(5), 599-605. https://doi.org/10.1016/j.pbi.2009.07.005

Bhosale, R., Boudolf, V., Cuevas, F., Lu, R., Eekhout, T., Hu, Z., Van Isterdael, G., Lambert, G. M., Xu, F., Nowack, M. K., Smith, R. S., Vercauteren, I., De Rycke, R., Storme, V., Beeckman, T., Larkin, J. C., Kremer, A., Hofte, H., Galbraith, D. W., … De Veylder, L. (2018). A Spatiotemporal DNA Endoploidy Map of the Arabidopsis Root Reveals Roles for

855 the Endocycle in Root Development and Stress Adaptation. *Plant Cell*, *30*(10), 2330-2351.
856 https://doi.org/10.1105/tpc.17.00983
857 Binder, A., Lambert, J., Morbitzer, R., Popp, C., Ott, T., Lahaye, T., & Parniske, M. (2014). A
858 modular plasmid assembly kit for multigene expression, gene silencing and silencing rescue
859 in plants. *PLoS One*, *9*(2), e88218. https://doi.org/10.1371/journal.pone.0088218
860 Boisson-Dernier, A., Chabaud, M., Garcia, F., Becard, G., Rosenberg, C., & Barker, D. G. (2001).
861 Agrobacterium rhizogenes-transformed roots of Medicago truncatula for the study of
862 nitrogen-fixing and endomycorrhizal symbiotic associations. *Mol Plant Microbe Interact*,
863 *14*(6), 695-700. https://doi.org/10.1094/MPMI.2001.14.6.695
864 Breakspear, A., Liu, C., Roy, S., Stacey, N., Rogers, C., Trick, M., Morieri, G., Mysore, K. S.,
865 Wen, J., Oldroyd, G. E., Downie, J. A., & Murray, J. D. (2014). The root hair « infectome »
866 of Medicago truncatula uncovers changes in cell cycle genes and reveals a requirement for
867 Auxin signaling in rhizobial infection. *Plant Cell*, *26*(12), 4680-4701.
868 https://doi.org/10.1105/tpc.114.133496
869 Bu, F., Rutten, L., Roswanjaya, Y. P., Kulikova, O., Rodriguez-Franco, M., Ott, T., Bisseling, T.,
870 van Zeijl, A., & Geurts, R. (2020). Mutant analysis in the nonlegume Parasponia andersonii
871 identifies NIN and NF-YA1 transcription factors as a core genetic network in nitrogen-
872 fixing nodule symbioses. *New Phytol*, *226*(2), 541-554. https://doi.org/10.1111/nph.16386
873 Carotenuto, G., Sciascia, I., Oddi, L., Volpe, V., & Genre, A. (2019b). Size matters : Three methods
874 for estimating nuclear size in mycorrhizal roots of Medicago truncatula by image analysis.
875 *BMC Plant Biol*, *19*(1), 180. https://doi.org/10.1186/s12870-019-1791-1
876 Carotenuto, G., Volpe, V., Russo, G., Politi, M., Sciascia, I., de Almeida-Engler, J., & Genre, A.
877 (2019a). Local endoreduplication as a feature of intracellular fungal accommodation in
878 arbuscular mycorrhizas. *New Phytol*, *223*(1), 430-446. https://doi.org/10.1111/nph.15763
879 Carrere, S., Verdier, J., & Gamas, P. (2021). MtExpress, a Comprehensive and Curated RNAseq-
880 based Gene Expression Atlas for the Model Legume Medicago truncatula. *Plant Cell*
881 *Physiol*, *62*(9), 1494-1500. https://doi.org/10.1093/pcp/pcab110
882 Cathebras, C., Gong, X., Andrade, R. E., Vondenhoff, K., Keller, J., Delaux, P.-M., Hayashi, M.,
883 Griesmann, M., & Parniske, M. (2022). *A novel cis-element enabled bacterial uptake by*
884 *plant cells* (p. 2022.03.28.486070). bioRxiv. https://doi.org/10.1101/2022.03.28.486070
885 Chen, P., Takatsuka, H., Takahashi, N., Kurata, R., Fukao, Y., Kobayashi, K., Ito, M., & Umeda,
886 M. (2017). Arabidopsis R1R2R3-Myb proteins are essential for inhibiting cell division in
887 response to DNA damage. *Nature Communications*, *8*(1), Article 1.
888 https://doi.org/10.1038/s41467-017-00676-4

889 Combier, J. P., Frugier, F., de Billy, F., Boualem, A., El-Yahyaoui, F., Moreau, S., Vernie, T., Ott,
890 T., Gamas, P., Crespi, M., & Niebel, A. (2006). MtHAP2-1 is a key transcriptional regulator
891 of symbiotic nodule development regulated by microRNA169 in Medicago truncatula.
892 *Genes Dev*, *20*(22), 3084-3088. https://doi.org/10.1101/gad.402806
893 Cosolo, A., Jaiswal, J., Csordas, G., Grass, I., Uhlirova, M., & Classen, A. K. (2019). JNK-
894 dependent cell cycle stalling in G2 promotes survival and senescence-like phenotypes in
895 tissue stress. *Elife*, *8*. https://doi.org/10.7554/eLife.41036
896 Costa, S. (2017). Are division plane determination and cell-cycle progression coordinated? *New*
897 *Phytol*, *213*(1), 16-21. https://doi.org/10.1111/nph.14261
898 Davarinejad, H., Huang, Y. C., Mermaz, B., LeBlanc, C., Poulet, A., Thomson, G., Joly, V.,
899 Munoz, M., Arvanitis-Vigneault, A., Valsakumar, D., Villarino, G., Ross, A., Rotstein, B.
900 H., Alarcon, E. I., Brunzelle, J. S., Voigt, P., Dong, J., Couture, J. F., & Jacob, Y. (2022).
901 The histone H3.1 variant regulates TONSOKU-mediated DNA repair during replication.
902 *Science*, *375*(6586), 1281-1286. https://doi.org/10.1126/science.abm5320
903 De Storme, N., Keceli, B. N., Zamariola, L., Angenon, G., & Geelen, D. (2016). CENH3-GFP: a
904 visual marker for gametophytic and somatic ploidy determination in Arabidopsis thaliana.
905 *BMC Plant Biol*, *16*, 1. https://doi.org/10.1186/s12870-015-0700-5
906 De Veylder, L., Larkin, J. C., & Schnittger, A. (2011). Molecular control and function of
907 endoreplication in development and physiology. *Trends Plant Sci*, *16*(11), 624-634.
908 https://doi.org/10.1016/j.tplants.2011.07.001
909 Desvoyes, B., Arana-Echarri, A., Barea, M. D., & Gutierrez, C. (2020). A comprehensive
910 fluorescent sensor for spatiotemporal cell cycle analysis in Arabidopsis. *Nat Plants*, *6*(11),
911 1330-1334. https://doi.org/10.1038/s41477-020-00770-4
912 Desvoyes, B., Noir, S., Masoud, K., López, M. I., Genschik, P., & Gutierrez, C. (2019). *FBL17*
913 *targets CDT1a for degradation in early S-phase to prevent Arabidopsis genome instability*
914 (p. 774109). bioRxiv. https://doi.org/10.1101/774109
915 Dewitte, W., Riou-Khamlichi, C., Scofield, S., Healy, J. M. S., Jacqmard, A., Kilby, N. J., &
916 Murray, J. A. H. (2003). Altered Cell Cycle Distribution, Hyperplasia, and Inhibited
917 Differentiation in Arabidopsis Caused by the D-Type Cyclin CYCD3. *The Plant Cell*, *15*(1),
918 79-92. https://doi.org/10.1105/tpc.004838
919 Dong, W., Zhu, Y., Chang, H., Wang, C., Yang, J., Shi, J., Gao, J., Yang, W., Lan, L., Wang, Y.,
920 Zhang, X., Dai, H., Miao, Y., Xu, L., He, Z., Song, C., Wu, S., Wang, D., Yu, N., & Wang,
921 E. (2021). An SHR-SCR module specifies legume cortical cell fate to enable nodulation.
922 *Nature*, *589*(7843), 586-590. https://doi.org/10.1038/s41586-020-3016-z

923 Draizen, E. J., Shaytan, A. K., Marino-Ramirez, L., Talbert, P. B., Landsman, D., & Panchenko, A.
924 R. (2016). HistoneDB 2.0 : A histone database with variants—An integrated resource to
925 explore histones and their variants. *Database (Oxford)*, *2016*.
926 https://doi.org/10.1093/database/baw014
927 Echevarría, C., Gutierrez, C., & Desvoyes, B. (2021). Tools for Assessing Cell-Cycle Progression
928 in Plants. *Plant and Cell Physiology*, *62*(8), 1231-1238. https://doi.org/10.1093/pcp/pcab066
929 Edgar, B. A., Zielke, N., & Gutierrez, C. (2014). Endocycles : A recurrent evolutionary innovation
930 for post-mitotic cell growth. *Nat Rev Mol Cell Biol*, *15*(3), 197-210.
931 https://doi.org/10.1038/nrm3756
932 Feng, J., Lee, T., Schiessl, K., & Oldroyd, G. E. D. (2021). Processing of NODULE INCEPTION
933 controls the transition to nitrogen fixation in root nodules. *Science*, *374*(6567), 629-632.
934 https://doi.org/10.1126/science.abg2804
935 Foucher, F., & Kondorosi, E. (2000). Cell cycle regulation in the course of nodule organogenesis in
936 Medicago. *Plant Mol Biol*, *43*(5-6), 773-786. https://doi.org/10.1023/a:1006405029600
937 Fournier, J., Teillet, A., Chabaud, M., Ivanov, S., Genre, A., Limpens, E., de Carvalho-Niebel, F.,
938 & Barker, D. G. (2015). Remodeling of the infection chamber before infection thread
939 formation reveals a two-step mechanism for rhizobial entry into the host legume root hair.
940 *Plant Physiol*, *167*(4), 1233-1242. https://doi.org/10.1104/pp.114.253302
941 Gao, J. P., Jiang, S., Su, Y., Xu, P., Wang, J., Liang, W., Liu, C. W., & Murray, J. D. (2022).
942 Intracellular infection by symbiotic bacteria requires the mitotic kinase AURORA1. *Proc*
943 *Natl Acad Sci U S A*, *119*(43), e2202606119. https://doi.org/10.1073/pnas.2202606119
944 Gaudioso-Pedraza, R., Beck, M., Frances, L., Kirk, P., Ripodas, C., Niebel, A., Oldroyd, G. E. D.,
945 Benitez-Alfonso, Y., & de Carvalho-Niebel, F. (2018). Callose-Regulated Symplastic
946 Communication Coordinates Symbiotic Root Nodule Development. *Curr Biol*, *28*(22),
947 3562-3577 e6. https://doi.org/10.1016/j.cub.2018.09.031
948 Gauthier-Coles, C., White, R. G., & Mathesius, U. (2018). Nodulating Legumes Are Distinguished
949 by a Sensitivity to Cytokinin in the Root Cortex Leading to Pseudonodule Development.
950 *Front Plant Sci*, *9*, 1901. https://doi.org/10.3389/fpls.2018.01901
951 Gigli-Bisceglia, N., Engelsdorf, T., Strnad, M., Vaahtera, L., Khan, G. A., Yamoune, A., Alipanah,
952 L., Novak, O., Persson, S., Hejatko, J., & Hamann, T. (2018). Cell wall integrity modulates
953 Arabidopsis thaliana cell cycle gene expression in a cytokinin- and nitrate reductase-
954 dependent manner. *Development*, *145*(19). https://doi.org/10.1242/dev.166678

955 Gleason, C., Chaudhuri, S., Yang, T., Munoz, A., Poovaiah, B. W., & Oldroyd, G. E. (2006).
956 Nodulation independent of rhizobia induced by a calcium-activated kinase lacking
957 autoinhibition. *Nature*, *441*(7097), 1149-1152. https://doi.org/10.1038/nature04812
958 Guan, D., Stacey, N., Liu, C., Wen, J., Mysore, K. S., Torres-Jerez, I., Vernié, T., Tadege, M.,
959 Zhou, C., Wang, Z., Udvardi, M. K., Oldroyd, G. E. D., & Murray, J. D. (2013). Rhizobial
960 Infection Is Associated with the Development of Peripheral Vasculature in Nodules of
961 Medicago truncatula. *Plant Physiology*, *162*(1), 107-115.
962 https://doi.org/10.1104/pp.113.215111
963 Haga, N., Kato, K., Murase, M., Araki, S., Kubo, M., Demura, T., Suzuki, K., Muller, I., Voss, U.,
964 Jurgens, G., & Ito, M. (2007). R1R2R3-Myb proteins positively regulate cytokinesis
965 through activation of KNOLLE transcription in Arabidopsis thaliana. *Development*, *134*(6),
966 1101-1110. https://doi.org/10.1242/dev.02801
967 Hayashi, T., Banba, M., Shimoda, Y., Kouchi, H., Hayashi, M., & Imaizumi-Anraku, H. (2010). A
968 dominant function of CCaMK in intracellular accommodation of bacterial and fungal
969 endosymbionts. *Plant J*, *63*(1), 141-154. https://doi.org/10.1111/j.1365-313X.2010.04228.x
970 Hernandez-Lagana, E., & Autran, D. (2020). H3.1 Eviction Marks Female Germline Precursors in
971 Arabidopsis. *Plants*, *9*(10), Article 10. https://doi.org/10.3390/plants9101322
972 Hernandez-Lagana, E., Mosca, G., Mendocilla-Sato, E., Pires, N., Frey, A., Giraldo-Fonseca, A.,
973 Michaud, C., Grossniklaus, U., Hamant, O., Godin, C., Boudaoud, A., Grimanelli, D.,
974 Autran, D., & Baroux, C. (2021). Organ geometry channels reproductive cell fate in the
975 Arabidopsis ovule primordium. *Elife*, *10*. https://doi.org/10.7554/eLife.66031
976 Hossain, M. S., Shrestha, A., Zhong, S., Miri, M., Austin, R. S., Sato, S., Ross, L., Huebert, T.,
977 Tromas, A., Torres-Jerez, I., Tang, Y., Udvardi, M., Murray, J. D., & Szczyglowski, K.
978 (2016). Lotus japonicus NF-YA1 Plays an Essential Role During Nodule Differentiation and
979 Targets Members of the SHI/STY Gene Family. *Mol Plant Microbe Interact*, *29*(12),
980 950-964. https://doi.org/10.1094/MPMI-10-16-0206-R
981 Imbriano, C., Gurtner, A., Cocchiarella, F., Di Agostino, S., Basile, V., Gostissa, M., Dobbelstein,
982 M., Del Sal, G., Piaggio, G., & Mantovani, R. (2005). Direct p53 transcriptional repression :
983 In vivo analysis of CCAAT-containing G2/M promoters. *Mol Cell Biol*, *25*(9), 3737-3751.
984 https://doi.org/10.1128/MCB.25.9.3737-3751.2005
985 Ingouff, M., Rademacher, S., Holec, S., Soljic, L., Xin, N., Readshaw, A., Foo, S. H., Lahouze, B.,
986 Sprunck, S., & Berger, F. (2010). Zygotic resetting of the HISTONE 3 variant repertoire
987 participates in epigenetic reprogramming in Arabidopsis. *Curr Biol*, *20*(23), 2137-2143.
988 https://doi.org/10.1016/j.cub.2010.11.012

989 Ito, M., Araki, S., Matsunaga, S., Itoh, T., Nishihama, R., Machida, Y., Doonan, J. H., & Watanabe,
990 A. (2001). G2/M-phase-specific transcription during the plant cell cycle is mediated by c-
991 Myb-like transcription factors. *Plant Cell*, *13*(8), 1891-1905.
992 https://doi.org/10.1105/tpc.010102
993 Iwata, E., Ikeda, S., Matsunaga, S., Kurata, M., Yoshioka, Y., Criqui, M. C., Genschik, P., & Ito,
994 M. (2011). GIGAS CELL1, a novel negative regulator of the anaphase-promoting
995 complex/cyclosome, is required for proper mitotic progression and cell fate determination in
996 Arabidopsis. *Plant Cell*, *23*(12), 4382-4393. https://doi.org/10.1105/tpc.111.092049
997 Jiang, D., & Berger, F. (2017). DNA replication–coupled histone modification maintains Polycomb
998 gene silencing in plants. *Science*, *357*(6356), 1146-1149.
999 https://doi.org/10.1126/science.aan4965
1000 Knaack, S. A., Conde, D., Chakraborty, S., Balmant, K. M., Irving, T. B., Maia, L. G. S., Triozzi, P.
1001 M., Dervinis, C., Pereira, W. J., Maeda, J., Schmidt, H. W., Ane, J. M., Kirst, M., & Roy, S.
1002 (2022). Temporal change in chromatin accessibility predicts regulators of nodulation in
1003 Medicago truncatula. *BMC Biol*, *20*(1), 252. https://doi.org/10.1186/s12915-022-01450-9
1004 Kobayashi, K., Suzuki, T., Iwata, E., Nakamichi, N., Suzuki, T., Chen, P., Ohtani, M., Ishida, T.,
1005 Hosoya, H., Müller, S., Leviczky, T., Pettkó-Szandtner, A., Darula, Z., Iwamoto, A.,
1006 Nomoto, M., Tada, Y., Higashiyama, T., Demura, T., Doonan, J. H., … Ito, M. (2015).
1007 Transcriptional repression by MYB3R proteins regulates plant organ growth. *The EMBO*
1008 *Journal*, *34*(15), 1992-2007. https://doi.org/10.15252/embj.201490899
1009 Kondorosi, E., & Kondorosi, A. (2004). Endoreduplication and activation of the anaphase-
1010 promoting complex during symbiotic cell development. *FEBS Lett*, *567*(1), 152-157.
1011 https://doi.org/10.1016/j.febslet.2004.04.075
1012 Lace, B., Su, C., Invernot Perez, D., Rodriguez-Franco, M., Vernie, T., Batzenschlager, M., Egli, S.,
1013 Liu, C. W., & Ott, T. (2023). RPG acts as a central determinant for infectosome formation
1014 and cellular polarization during intracellular rhizobial infections. *Elife*, *12*.
1015 https://doi.org/10.7554/eLife.80741
1016 Laloum, T., Baudin, M., Frances, L., Lepage, A., Billault-Penneteau, B., Cerri, M. R., Ariel, F.,
1017 Jardinaud, M.-F., Gamas, P., de Carvalho-Niebel, F., & Niebel, A. (2014). Two CCAAT-
1018 box-binding transcription factors redundantly regulate early steps of the legume-rhizobia
1019 endosymbiosis. *The Plant Journal*, *79*(5), 757-768. https://doi.org/10.1111/tpj.12587
1020 Laporte, P., Lepage, A., Fournier, J., Catrice, O., Moreau, S., Jardinaud, M. F., Mun, J. H.,
1021 Larrainzar, E., Cook, D. R., Gamas, P., & Niebel, A. (2014). The CCAAT box-binding

1022 transcription factor NF-YA1 controls rhizobial infection. *J Exp Bot*, *65*(2), 481-494.
1023 https://doi.org/10.1093/jxb/ert392
1024 Lermontova, I., Fuchs, J., Schubert, V., & Schubert, I. (2007). Loading time of the centromeric
1025 histone H3 variant differs between plants and animals. *Chromosoma*, *116*(6), 507-510.
1026 https://doi.org/10.1007/s00412-007-0122-8
1027 Lermontova, I., Rutten, T., & Schubert, I. (2011). Deposition, turnover, and release of CENH3 at
1028 Arabidopsis centromeres. *Chromosoma*, *120*(6), 633-640. https://doi.org/10.1007/s00412-
1029 011-0338-5
1030 Lermontova, I., Schubert, V., Fuchs, J., Klatte, S., Macas, J., & Schubert, I. (2006). Loading of
1031 Arabidopsis centromeric histone CENH3 occurs mainly during G2 and requires the presence
1032 of the histone fold domain. *Plant Cell*, *18*(10), 2443-2451.
1033 https://doi.org/10.1105/tpc.106.043174
1034 Liang, J., Klingl, A., Lin, Y.-Y., Boul, E., Thomas-Oates, J., & Marín, M. (2019). A subcompatible
1035 rhizobium strain reveals infection duality in Lotus. *Journal of Experimental Botany*, *70*(6),
1036 1903-1913. https://doi.org/10.1093/jxb/erz057
1037 Libbenga, K. R., & Torrey, J. G. (1973). Hormone-Induced Endoreduplication Prior to Mitosis in
1038 Cultured Pea Root Cortex Cells. *American Journal of Botany*, *60*(4), 293-299.
1039 https://doi.org/10.2307/2441195
1040 Linhart, C., Elkon, R., Shiloh, Y., & Shamir, R. (2005). Deciphering transcriptional regulatory
1041 elements that encode specific cell cycle phasing by comparative genomics analysis. *Cell*
1042 *Cycle*, *4*(12), 1788-1797. https://doi.org/10.4161/cc.4.12.2173
1043 Liu, C. W., Breakspear, A., Stacey, N., Findlay, K., Nakashima, J., Ramakrishnan, K., Liu, M., Xie,
1044 F., Endre, G., de Carvalho-Niebel, F., Oldroyd, G. E. D., Udvardi, M. K., Fournier, J., &
1045 Murray, J. D. (2019a). A protein complex required for polar growth of rhizobial infection
1046 threads. *Nat Commun*, *10*(1), 2848. https://doi.org/10.1038/s41467-019-10029-y
1047 Liu, H., Lin, J.-S., Luo, Z., Sun, J., Huang, X., Yang, Y., Xu, J., Wang, Y.-F., Zhang, P., Oldroyd,
1048 G. E. D., & Xie, F. (2022). Constitutive activation of a nuclear-localized calcium channel
1049 complex in Medicago truncatula. *Proceedings of the National Academy of Sciences*,
1050 *119*(34), e2205920119. https://doi.org/10.1073/pnas.2205920119
1051 Liu, J., Rutten, L., Limpens, E., van der Molen, T., van Velzen, R., Chen, R., Chen, Y., Geurts, R.,
1052 Kohlen, W., Kulikova, O., & Bisseling, T. (2019b). A Remote cis-Regulatory Region Is
1053 Required for NIN Expression in the Pericycle to Initiate Nodule Primordium Formation in
1054 Medicago truncatula. *Plant Cell*, *31*(1), 68-83. https://doi.org/10.1105/tpc.18.00478

Ma, Y., Jonsson, K., Aryal, B., De Veylder, L., Hamant, O., & Bhalerao, R. P. (2022). Endoreplication mediates cell size control via mechanochemical signaling from cell wall. *Sci Adv*, *8*(49), eabq2047. https://doi.org/10.1126/sciadv.abq2047

Manni, I., Mazzaro, G., Gurtner, A., Mantovani, R., Haugwitz, U., Krause, K., Engeland, K., Sacchi, A., Soddu, S., & Piaggio, G. (2001). NF-Y mediates the transcriptional inhibition of the cyclin B1, cyclin B2, and cdc25C promoters upon induced G2 arrest. *J Biol Chem*, *276*(8), 5570-5576. https://doi.org/10.1074/jbc.M006052200

Marsh, J. F., Rakocevic, A., Mitra, R. M., Brocard, L., Sun, J., Eschstruth, A., Long, S. R., Schultze, M., Ratet, P., & Oldroyd, G. E. (2007). Medicago truncatula NIN is essential for rhizobial-independent nodule organogenesis induced by autoactive calcium/calmodulin-dependent protein kinase. *Plant Physiol*, *144*(1), 324-335. https://doi.org/10.1104/pp.106.093021

McCloy, R. A., Rogers, S., Caldon, C. E., Lorca, T., Castro, A., & Burgess, A. (2014). Partial inhibition of Cdk1 in G 2 phase overrides the SAC and decouples mitotic events. *Cell Cycle*, *13*(9), 1400-1412. https://doi.org/10.4161/cc.28401

Meserve, J. H., & Duronio, R. J. (2017). A population of G2-arrested cells are selected as sensory organ precursors for the interommatidial bristles of the Drosophila eye. *Dev Biol*, *430*(2), 374-384. https://doi.org/10.1016/j.ydbio.2017.06.023

Mutterer, J., & Zinck, E. (2013). Quick-and-clean article figures with FigureJ. *J Microsc*, *252*(1), 89-91. https://doi.org/10.1111/jmi.12069

Myers, Z. A., & Holt, B. F. (2018). NUCLEAR FACTOR-Y: still complex after all these years? *Curr Opin Plant Biol*, *45*(Pt A), 96-102. https://doi.org/10.1016/j.pbi.2018.05.015

Nadzieja, M., Stougaard, J., & Reid, D. (2019). A Toolkit for High Resolution Imaging of Cell Division and Phytohormone Signaling in Legume Roots and Root Nodules. *Front Plant Sci*, *10*, 1000. https://doi.org/10.3389/fpls.2019.01000

Nagymihaly, M., Veluchamy, A., Gyorgypal, Z., Ariel, F., Jegu, T., Benhamed, M., Szucs, A., Kereszt, A., Mergaert, P., & Kondorosi, E. (2017). Ploidy-dependent changes in the epigenome of symbiotic cells correlate with specific patterns of gene expression. *Proc Natl Acad Sci U S A*, *114*(17), 4543-4548. https://doi.org/10.1073/pnas.1704211114

Negishi, T., Veis, J., Hollenstein, D., Sekiya, M., Ammerer, G., & Ohya, Y. (2016). The Late S-Phase Transcription Factor Hcm1 Is Regulated through Phosphorylation by the Cell Wall Integrity Checkpoint. *Mol Cell Biol*, *36*(6), 941-953. https://doi.org/10.1128/MCB.00952-15

1087 Otero, S., Desvoyes, B., Peiro, R., & Gutierrez, C. (2016). Histone H3 Dynamics Reveal Domains
1088 with Distinct Proliferation Potential in the Arabidopsis Root. *Plant Cell*, *28*(6), 1361-1371.
1089 https://doi.org/10.1105/tpc.15.01003
1090 Parniske, M. (2018). Uptake of bacteria into living plant cells, the unifying and distinct feature of
1091 the nitrogen-fixing root nodule symbiosis. *Curr Opin Plant Biol*, *44*, 164-174.
1092 https://doi.org/10.1016/j.pbi.2018.05.016
1093 Probst, A. V., Desvoyes, B., & Gutierrez, C. (2020). Similar yet critically different : The
1094 distribution, dynamics and function of histone variants. *J Exp Bot*, *71*(17), 5191-5204.
1095 https://doi.org/10.1093/jxb/eraa230
1096 Procter, J. B., Carstairs, G. M., Soares, B., Mourao, K., Ofoegbu, T. C., Barton, D., Lui, L.,
1097 Menard, A., Sherstnev, N., Roldan-Martinez, D., Duce, S., Martin, D. M. A., & Barton, G. J.
1098 (2021). Alignment of Biological Sequences with Jalview. *Methods Mol Biol*, *2231*, 203-224.
1099 https://doi.org/10.1007/978-1-0716-1036-7_13
1100 Rost, T. L. (2011). The organization of roots of dicotyledonous plants and the positions of control
1101 points. *Ann Bot*, *107*(7), 1213-1222. https://doi.org/10.1093/aob/mcq229
1102 Roux, B., Rodde, N., Jardinaud, M. F., Timmers, T., Sauviac, L., Cottret, L., Carrere, S., Sallet, E.,
1103 Courcelle, E., Moreau, S., Debelle, F., Capela, D., de Carvalho-Niebel, F., Gouzy, J.,
1104 Bruand, C., & Gamas, P. (2014). An integrated analysis of plant and bacterial gene
1105 expression in symbiotic root nodules using laser-capture microdissection coupled to RNA
1106 sequencing. *Plant J*, *77*(6), 817-837. https://doi.org/10.1111/tpj.12442
1107 Russo, G., Carotenuto, G., Fiorilli, V., Volpe, V., Chiapello, M., Van Damme, D., & Genre, A.
1108 (2019). Ectopic activation of cortical cell division during the accommodation of arbuscular
1109 mycorrhizal fungi. *New Phytol*, *221*(2), 1036-1048. https://doi.org/10.1111/nph.15398
1110 Russo, G., & Genre, A. (2021). Divide and Be Conquered-Cell Cycle Reactivation in Arbuscular
1111 Mycorrhizal Symbiosis. *Front Plant Sci*, *12*, 753265.
1112 https://doi.org/10.3389/fpls.2021.753265
1113 Schiessl, K., Lee, T., Orvosova, M., Bueno-Batista, M., Stuer, N., Bailey, P. C., Mysore, K. S.,
1114 Wen, J., & Oldroyd, G. E. D. (2023). *Light sensitive short hypocotyl (LSH) confer symbiotic*
1115 *nodule identity in the legume Medicago truncatula* (p. 2023.02.12.528179). bioRxiv.
1116 https://doi.org/10.1101/2023.02.12.528179
1117 Schiessl, K., Lilley, J. L. S., Lee, T., Tamvakis, I., Kohlen, W., Bailey, P. C., Thomas, A., Luptak,
1118 J., Ramakrishnan, K., Carpenter, M. D., Mysore, K. S., Wen, J., Ahnert, S., Grieneisen, V.
1119 A., & Oldroyd, G. E. D. (2019). NODULE INCEPTION Recruits the Lateral Root

1120 Developmental Program for Symbiotic Nodule Organogenesis in Medicago truncatula. *Curr*
1121 *Biol*, *29*(21), 3657-3668 e5. https://doi.org/10.1016/j.cub.2019.09.005
1122 Schindelin, J., Arganda-Carreras, I., Frise, E., Kaynig, V., Longair, M., Pietzsch, T., Preibisch, S.,
1123 Rueden, C., Saalfeld, S., Schmid, B., Tinevez, J. Y., White, D. J., Hartenstein, V., Eliceiri,
1124 K., Tomancak, P., & Cardona, A. (2012). Fiji : An open-source platform for biological-
1125 image analysis. *Nat Methods*, *9*(7), 676-682. https://doi.org/10.1038/nmeth.2019
1126 Schnittger, A., Schöbinger, U., Bouyer, D., Weinl, C., Stierhof, Y.-D., & Hülskamp, M. (2002).
1127 Ectopic D-type cyclin expression induces not only DNA replication but also cell division in
1128 Arabidopsis trichomes. *Proceedings of the National Academy of Sciences of the United*
1129 *States of America*, *99*(9), 6410-6415. https://doi.org/10.1073/pnas.092657299
1130 Shi, L., Wang, J., Hong, F., Spector, D. L., & Fang, Y. (2011). Four amino acids guide the
1131 assembly or disassembly of Arabidopsis histone H3.3-containing nucleosomes. *Proceedings*
1132 *of the National Academy of Sciences*, *108*(26), 10574-10578.
1133 https://doi.org/10.1073/pnas.1017882108
1134 Silhavy, D., Molnar, A., Lucioli, A., Szittya, G., Hornyik, C., Tavazza, M., & Burgyan, J. (2002). A
1135 viral protein suppresses RNA silencing and binds silencing-generated, 21- to 25-nucleotide
1136 double-stranded RNAs. *EMBO J*, *21*(12), 3070-3080. https://doi.org/10.1093/emboj/cdf312
1137 Singh, S., Katzer, K., Lambert, J., Cerri, M., & Parniske, M. (2014). CYCLOPS, a DNA-binding
1138 transcriptional activator, orchestrates symbiotic root nodule development. *Cell Host*
1139 *Microbe*, *15*(2), 139-152. https://doi.org/10.1016/j.chom.2014.01.011
1140 Soyano, T., Hirakawa, H., Sato, S., Hayashi, M., & Kawaguchi, M. (2014). Nodule Inception
1141 creates a long-distance negative feedback loop involved in homeostatic regulation of nodule
1142 organ production. *Proc Natl Acad Sci U S A*, *111*(40), 14607-14612.
1143 https://doi.org/10.1073/pnas.1412716111
1144 Soyano, T., Kouchi, H., Hirota, A., & Hayashi, M. (2013). Nodule inception directly targets NF-Y
1145 subunit genes to regulate essential processes of root nodule development in Lotus japonicus.
1146 *PLoS Genet*, *9*(3), e1003352. https://doi.org/10.1371/journal.pgen.1003352
1147 Su, C., Zhang, G., Rodriguez-Franco, M., Hinnenberg, R., Wietschorke, J., Liang, P., Yang, W.,
1148 Uhler, L., Li, X., & Ott, T. (2023). Transcellular progression of infection threads in
1149 Medicago truncatula roots is associated with locally confined cell wall modifications. *Curr*
1150 *Biol*, *33*(3), 533-542 e5. https://doi.org/10.1016/j.cub.2022.12.051
1151 Suzaki, T., Ito, M., Yoro, E., Sato, S., Hirakawa, H., Takeda, N., & Kawaguchi, M. (2014).
1152 Endoreduplication-mediated initiation of symbiotic organ development in Lotus japonicus.
1153 *Development*, *141*(12), 2441-2445. https://doi.org/10.1242/dev.107946

1154 Takahashi, N., Ogita, N., Takahashi, T., Taniguchi, S., Tanaka, M., Seki, M., & Umeda, M. (2019).
1155 A regulatory module controlling stress-induced cell cycle arrest in Arabidopsis. *Elife*, *8*.
1156 https://doi.org/10.7554/eLife.43944
1157 Timmers, A. C., Auriac, M. C., & Truchet, G. (1999). Refined analysis of early symbiotic steps of
1158 the Rhizobium-Medicago interaction in relationship with microtubular cytoskeleton
1159 rearrangements. *Development*, *126*(16), 3617-3628. https://doi.org/10.1242/dev.126.16.3617
1160 Torrey, J. G., & Barrios, S. (1969). Cytological Studies on Rhizobial Nodule Initiation in Pisum.
1161 *Caryologia*, *22*(1), 47-61. https://doi.org/10.1080/00087114.1969.10796324
1162 Trolet, A., Baldrich, P., Criqui, M. C., Dubois, M., Clavel, M., Meyers, B. C., & Genschik, P.
1163 (2019). Cell Cycle-Dependent Regulation and Function of ARGONAUTE1 in Plants. *Plant*
1164 *Cell*, *31*(8), 1734-1750. https://doi.org/10.1105/tpc.19.00069
1165 Tsyganova, A. V., Brewin, N. J., & Tsyganov, V. E. (2021). Structure and Development of the
1166 Legume-Rhizobial Symbiotic Interface in Infection Threads. *Cells*, *10*(5).
1167 https://doi.org/10.3390/cells10051050
1168 Ursache, R., Andersen, T. G., Marhavy, P., & Geldner, N. (2018). A protocol for combining
1169 fluorescent proteins with histological stains for diverse cell wall components. *Plant J*, *93*(2),
1170 399-412. https://doi.org/10.1111/tpj.13784
1171 van Brussel, A. A., Bakhuizen, R., van Spronsen, P. C., Spaink, H. P., Tak, T., Lugtenberg, B. J., &
1172 Kijne, J. W. (1992). Induction of pre-infection thread structures in the leguminous host plant
1173 by mitogenic lipo-oligosaccharides of Rhizobium. *Science*, *257*(5066), 70-72.
1174 https://doi.org/10.1126/science.257.5066.70
1175 Vinardell, J. M., Fedorova, E., Cebolla, A., Kevei, Z., Horvath, G., Kelemen, Z., Tarayre, S.,
1176 Roudier, F., Mergaert, P., Kondorosi, A., & Kondorosi, E. (2003). Endoreduplication
1177 mediated by the anaphase-promoting complex activator CCS52A is required for symbiotic
1178 cell differentiation in Medicago truncatula nodules. *Plant Cell*, *15*(9), 2093-2105.
1179 https://doi.org/10.1105/tpc.014373
1180 Weber, E., Engler, C., Gruetzner, R., Werner, S., & Marillonnet, S. (2011). A modular cloning
1181 system for standardized assembly of multigene constructs. *PloS One*, *6*(2), e16765.
1182 https://doi.org/10.1371/journal.pone.0016765
1183 Weimer, A. K., Biedermann, S., Harashima, H., Roodbarkelari, F., Takahashi, N., Foreman, J.,
1184 Guan, Y., Pochon, G., Heese, M., Van Damme, D., Sugimoto, K., Koncz, C., Doerner, P.,
1185 Umeda, M., & Schnittger, A. (2016). The plant-specific CDKB1-CYCB1 complex mediates
1186 homologous recombination repair in Arabidopsis. *EMBO J*, *35*(19), 2068-2086.
1187 https://doi.org/10.15252/embj.201593083

1188 Wildermuth, M. C., Steinwand, M. A., McRae, A. G., Jaenisch, J., & Chandran, D. (2017). Adapted
1189 Biotroph Manipulation of Plant Cell Ploidy. *Annu Rev Phytopathol*, *55*, 537-564.
1190 https://doi.org/10.1146/annurev-phyto-080516-035458
1191 Xiao, T. T., Schilderink, S., Moling, S., Deinum, E. E., Kondorosi, E., Franssen, H., Kulikova, O.,
1192 Niebel, A., & Bisseling, T. (2014). Fate map of Medicago truncatula root nodules.
1193 *Development*, *141*(18), 3517-3528. https://doi.org/10.1242/dev.110775
1194 Xiao, T. T., van Velzen, R., Kulikova, O., Franken, C., & Bisseling, T. (2019). Lateral root
1195 formation involving cell division in both pericycle, cortex and endodermis is a common and
1196 ancestral trait in seed plants. *Development (Cambridge, England)*, *146*(20), dev182592.
1197 https://doi.org/10.1242/dev.182592
1198 Xu, J., Lee, Y. J., & Liu, B. (2020). Establishment of a mitotic model system by transient
1199 expression of the D-type cyclin in differentiated leaf cells of tobacco (Nicotiana
1200 benthamiana). *New Phytol*, *226*(4), 1213-1220. https://doi.org/10.1111/nph.16309
1201 Yang, W. C., de Blank, C., Meskiene, I., Hirt, H., Bakker, J., van Kammen, A., Franssen, H., &
1202 Bisseling, T. (1994). Rhizobium nod factors reactivate the cell cycle during infection and
1203 nodule primordium formation, but the cycle is only completed in primordium formation.
1204 *Plant Cell*, *6*(10), 1415-1426. https://doi.org/10.1105/tpc.6.10.1415
1205 Yant, L., & Bomblies, K. (2015). Genome management and mismanagement—Cell-level
1206 opportunities and challenges of whole-genome duplication. *Genes Dev*, *29*(23), 2405-2419.
1207 https://doi.org/10.1101/gad.271072.115
1208 Zanetti, M. E., Ripodas, C., & Niebel, A. (2017). Plant NF-Y transcription factors : Key players in
1209 plant-microbe interactions, root development and adaptation to stress. *Biochim Biophys Acta*
1210 *Gene Regul Mech*, *1860*(5), 645-654. https://doi.org/10.1016/j.bbagrm.2016.11.007
1211
1212
1213

FIGURES

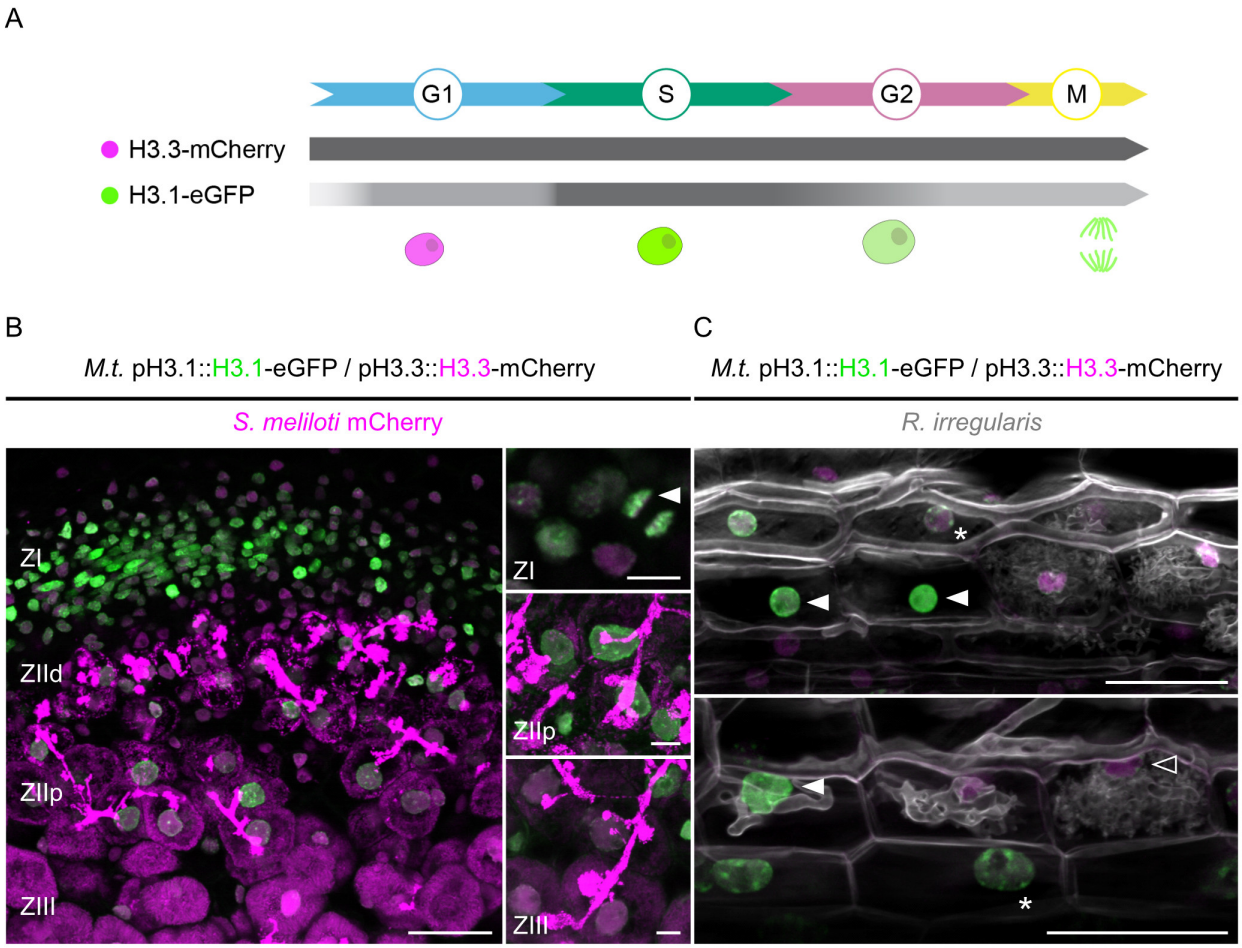

Figure 1. Medicago histone H3.1 patterns reveal sustained mitotic and endocycling activities in a symbiotic context. **(A)** Schematic representation of histone H3.3-mCherry and H3.1-eGFP distribution (horizontal bars) and fluorescence intensity (grey saturation) throughout the different cell-cycle phases (adapted from Echevarria et al., 2021). H3.1 is predominantly expressed during S-phase and incorporated during DNA replication in proliferating (G1, S, G2, M) and endocycling (G1, S, G2) cells. H3.3 is constitutively produced. Nuclei of increasing size and DNA content are coloured according to their H3.3 (pink) and H3.1 (green) content in decondensed chromatin (G1, S, G2) or condensed chromosomes (M). **(B)** Confocal images of nodule sections isolated from WT transgenic roots inoculated with mCherry-producing *S. meliloti* (35 to 40 dpi), showing H3.1-eGFP (green) and H3.3-mCherry (magenta) localization across characteristic developmental zones. H3.1 accumulates in the meristematic zone (ZI) enriched in proliferating cells (late-anaphase chromosomes indicated by a filled arrowhead) and in regions with high endoreduplication activity (ZIId and ZIIp, distal and proximal parts of the infection zone) where rhizobia are released into membrane-bound compartments called symbiosomes. H3.1 is extensively replaced by H3.3 in the fixation zone (ZIII) where host cells and rhizobia complete their differentiation process. Images are maximum intensity projections except the top-right panel (single focal plane). Scale bars: left panel = 50 µm; right panels = 10 µm. Transformation experiments were repeated 3 times with a total of 9 nodules from 6 composite plants showing similar results. **(C)** Confocal images of whole-mount WT roots colonized by *Rhizophagus irregularis* (15 dpi). Plant and fungal cell walls were stained with Calcofluor white (grayscale). H3.1 was enriched in chromocenters (heterochromatin foci in nuclei indicated by stars) and kept at high levels in the euchromatin (diffuse labeling in nuclei pointed by filled arrowheads) from neighbouring (upper panel) and early-arbusculated cells (lower panel) of the inner cortical tissue. The empty arrowhead points to a nucleus with a low H3.1 content in a fully-arbusculated, differentiated cell. Images are maximum intensity projections. Scale bars: 50 µm. Two independent transformation experiments were performed with 3 to 5 composite plants analyzed per replica.

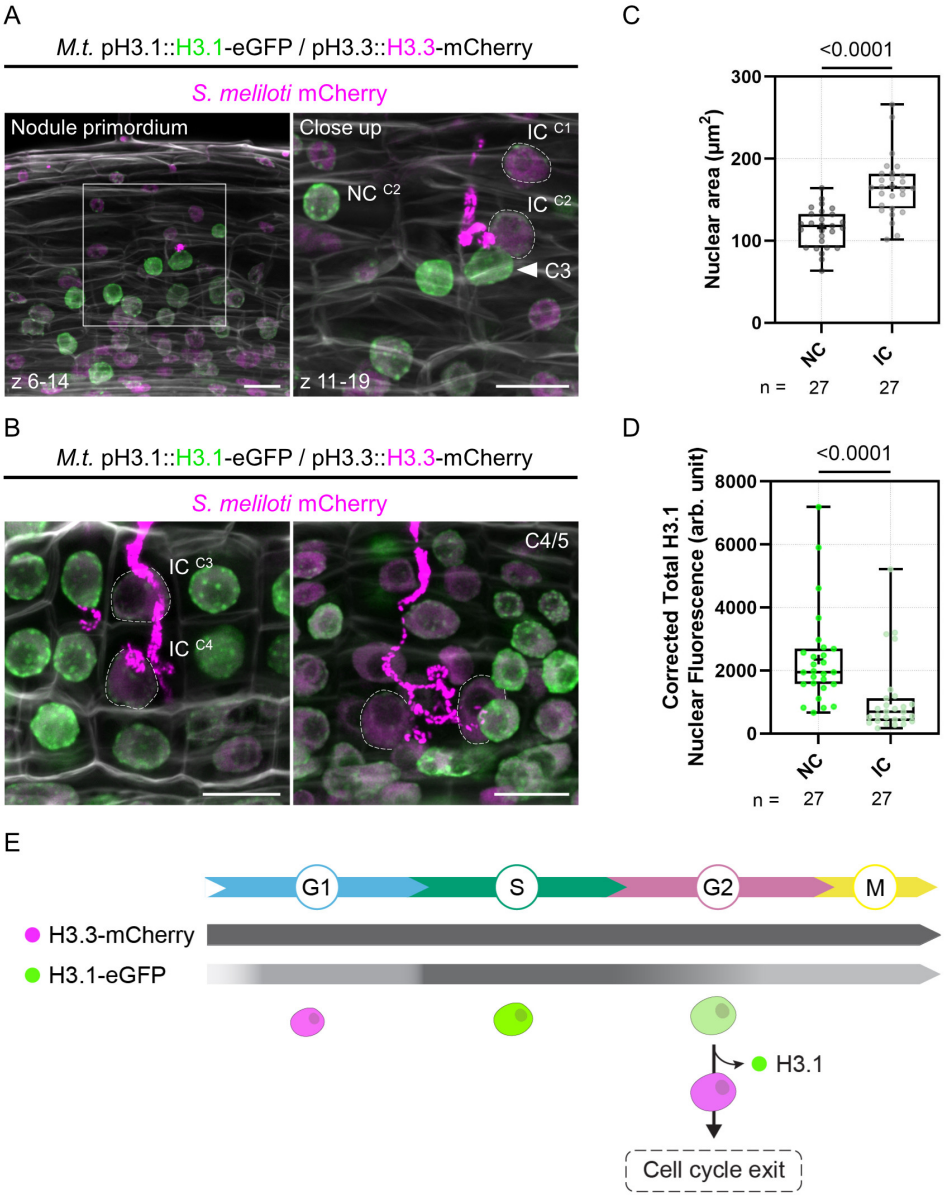

Figure 2. Individual reprogramming for infection includes large-scale chromatin rearrangements.
(**A-B**) Confocal images of whole-mount WT roots expressing the pH3.1::H3.1-eGFP / pH3.3::H3.3-mCherry reporter and inoculated with mCherry-producing *S. meliloti* (8 dpi). Images are maximum intensity projections (eGFP: green; mCherry: magenta; Calcofluor white cell-wall staining: grayscale). (**A**) Left panel: the solid-line frame indicates the outer and middle cortical regions of an early nodule primordium shown in the close up. Right panel: dotted-line regions of interest (ROIs) indicate nuclei of infected cells (IC) fully passed by a cortical infection thread in the first (C1) and second (C2) cortical layers. NC: neighbouring cell. The filled arrowhead points to the nucleus of a host cell from the middle cortical layer (C3) which is just penetrated by the infection thread. Scale bars: 20 µm. (**B**) Left panel: dotted-line ROIs indicate nuclei of infected cells (IC) being passed (C4) or recently passed (C3) by a cortical infection thread. Right panel: dotted-line ROIs indicate nuclei of infected cells in the inner cortex (C4/5) of a nodule primordium with several cell layers. Scale bars: 20 µm. (**C-D**) Quantification of the nuclear area (**C**) and corrected total H3.1-eGFP nuclear fluorescence (**D**) at the equatorial plane in couples of neighbouring (NC) and infected cells (IC) from the same cortical layer (C2 to C4, n = 27; see Materials and methods for more details). Roots from 2 to 7 composite plants with visible signs of inner cortical cell division (*i.e.*, showing high H3.1-eGFP signal) were analyzed from 3 independent transformation experiments. All data points are shown and crosses indicate sample means. Differences were statistically significant (p-values < 0.0001) using an unpaired t-test with Welch's correction (**C**) or a Mann-Whitney test (**D**). (**E**) Schematic representation of histone H3.3-mCherry and H3.1-eGFP distribution (horizontal bars) and fluorescence intensity (grey saturation) throughout the different cell-cycle phases. Nuclei of increasing size and DNA content are coloured according to their merged H3.3 (magenta) and H3.1 (green) content in decondensed chromatin (G1, S, G2). This diagram illustrates cells exiting the cell cycle within proliferating or endoreduplicating populations, which proceed to a massive H3.1 eviction following their last DNA replication round (Otero et al., 2016).

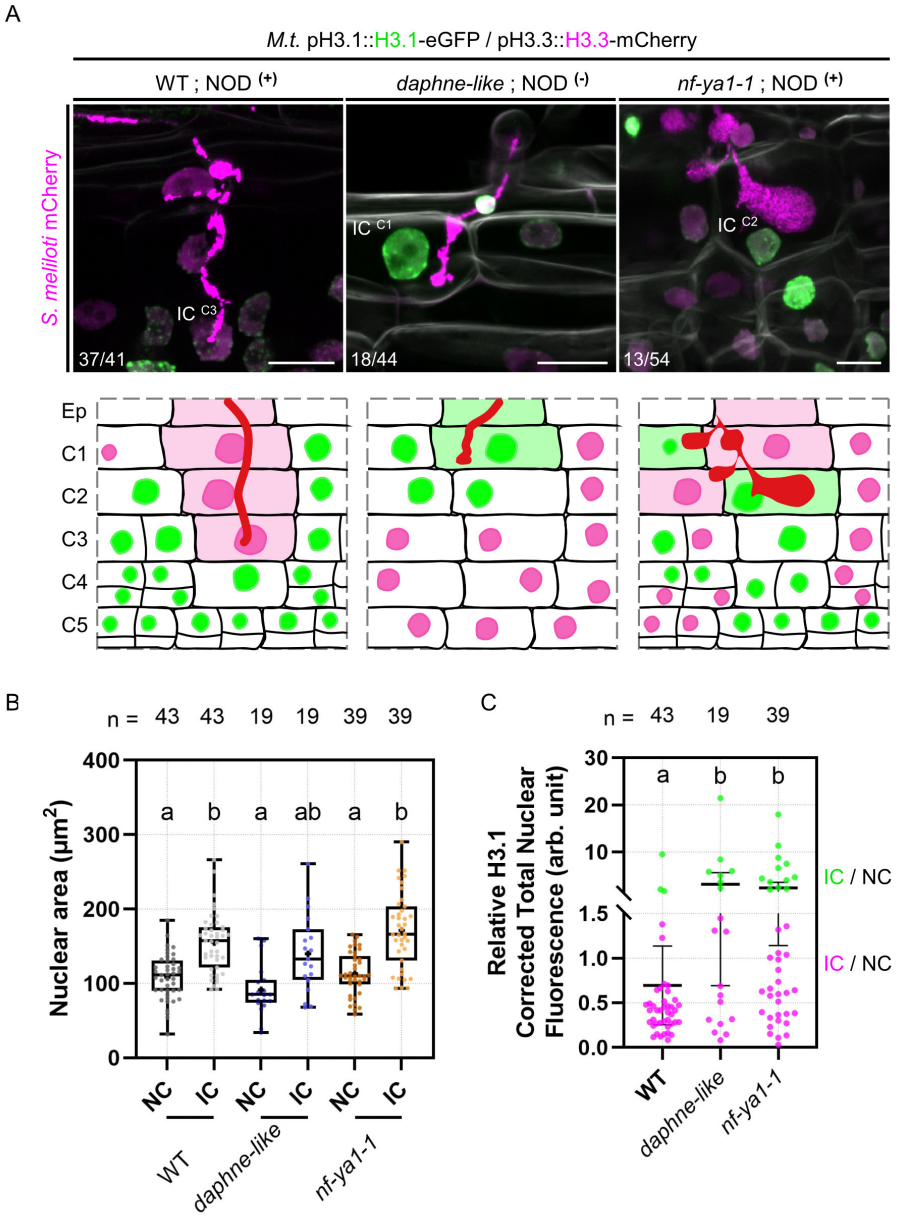

Figure 3. H3.1 eviction coincides with cortical infection thread progression.
(**A**) Confocal images of whole-mount transgenic roots co-expressing H3.1-eGFP and H3.3-mCherry in three different genotypes: WT (11 dpi), *daphne-like* (14 dpi) and *nf-ya1-1* (12 dpi), inoculated with mCherry-producing *S. meliloti*. WT and *nf-ya1-1* plants initiate nodule formation (NOD^+) whereas the *daphne-like* mutant is non-nodulating (NOD^-). Numbers indicate the frequencies of observation of a low (WT) or high (*daphne-like*, *nf-ya1-1*) H3.1-eGFP content in the last infected cortical cell. Corresponding schematic representations below each panel depict cellular proliferation or endocycling activities indicated by nuclear H3.1 levels (low: magenta; high: green) on the cortical infection thread trajectory (C1 to C3; diffuse magenta or green colouring) and in inner cortical layers (C4 to C5). Rhizobia inside infection threads are depicted in red. Confocal images are maximum intensity projections and show merged fluorescent channels (eGFP: green; mCherry: magenta; Calcofluor white cell-wall staining: grayscale in the middle and right panels). Scale bars: 20 µm. IC: infected cell. Ep: epidermis. (**B-C**) Quantification of the nuclear area (**B**) and the relative corrected total H3.1-eGFP nuclear fluorescence (IC/NC) (**C**) at the equatorial plane in couples of neighbouring (NC) and infected cells (IC) from the same cortical layer in WT (C1 to C4), *daphne-like* (C1 to C2) and *nf-ya1-1* (C1 to C4) genetic backgrounds (n = 43, 19 and 39 nuclei, respectively). Different letters indicate statistically significant differences according to a Kruskal-Wallis test followed by Dunn's multiple comparisons test. (**B**) All data points are shown and crosses indicate sample means. (**C**) All data points are shown with magenta or green indicating relative H3.1-eGFP nuclear signals (IC/NC) below 1,5 or above 1,6, respectively. Horizontal bars indicate sample means with 95% confidence interval. Ten to 21 composite plants (8-14 dpi) from 2 (*daphne-like*, *nf-ya1-1*) to 7 (WT) independent transformation experiments were analyzed.

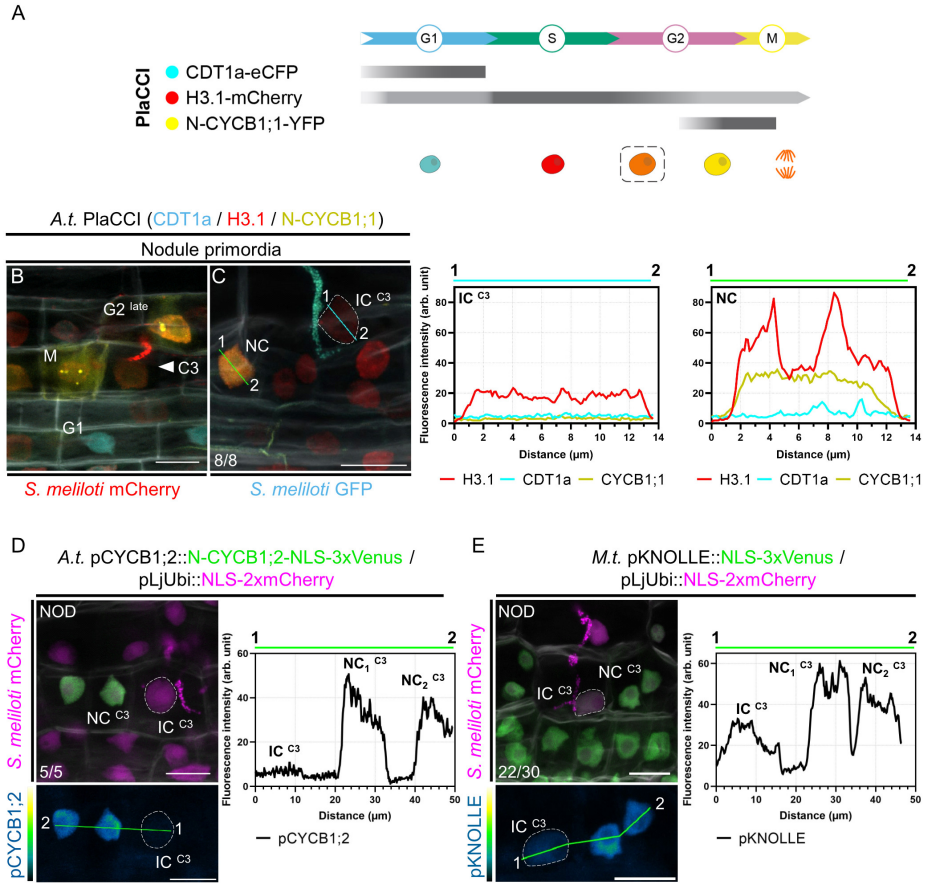

Figure 4. A tight control over host cells' mitotic commitment enables passage of the future nodule meristem.
(**A**) Schematic representation of Arabidopsis CDT1a-eCFP, H3.1-mCherry and N-CYCB1;1-YFP distribution (horizontal bars) and fluorescence intensity (grey saturation) throughout the different cell-cycle phases (adapted from Echevarria et al., 2021; see also Desvoyes et al., 2020). CDT1a-CFP accumulates in G1 and is rapidly degraded during the G1/S transition (blunt end bar). H3.1 is predominantly expressed during S-phase and incorporated during DNA replication. N-CYCB1;1-YFP is present in late G2 and mitotic cells and is completely degraded in anaphase (blunt end bar). Nuclei of increasing size and DNA content are coloured according to their CDT1a (cyan), H3.1 (red) and N-CYCB1;1 (yellow) content in/around decondensed chromatin (G1, S, G2) or condensed chromosomes (M). H3.1 levels decrease in differentiating cells (dotted-line box). (**B-C**) Confocal images of whole-mount Medicago WT roots expressing the Arabidopsis PlaCCI reporter in nodule primordia at 7 dpi with mCherry- (**B**) or GFP-producing *S. meliloti* (**C**). Images are maximum intensity projections and show merged fluorescent channels (eCFP and GFP: cyan; mCherry: red; YFP: yellow; Calcofluor white cell-wall staining: grayscale). (**B**) The filled arrowhead points to a cell of the C3 layer just penetrated by an infection thread. Cell-cycle phases of non-infected neighbouring cells are indicated. (**C**) Left panel: the dotted-line ROI indicates the nucleus of an infected cell (IC) from the C3 layer being passed by a cortical infection thread. Numbers indicate the frequencies of observation of the absence of CDT1a- or N-CYCB1;1-associated signals in the nucleus of the last infected cortical cell. Right panels: fluorescence intensity profiles of CDT1a-, H3.1- and N-CYCB1.1-associated signals along the cyan and green transects shown in (**C**). Scale bars: 20 µm. (**D**) Left panels: confocal images of a whole-mount WT root co-expressing a destabilized triple-Venus nuclear reporter driven by the Arabidopsis *CYCB1;2* promoter (pCYCB1;2::N-CYCB1;2-NLS-3xVenus) and a nuclear-localized tandem-mCherry as a transformation marker, 12 dpi with mCherry-producing *S. meliloti*. Numbers indicate the frequencies of observation of the absence of the triple-Venus reporter signal in the nucleus of the last infected cortical cell. Two independent transformation experiments were performed with 3 to 4 composite plants analyzed per replica. (**E**) Left panels: confocal images of a whole-mount WT root co-expressing a transcriptional reporter of Medicago *KNOLLE* driving a nuclear-localized triple-Venus (pKNOLLE::NLS-3xVenus) together with a nuclear-localized tandem-mCherry as a transformation marker, 12 dpi with mCherry-producing *S. meliloti*. Numbers indicate the frequencies of observation of nodule primordia where the triple-Venus reporter signal is kept comparably low on the cortical infection thread trajectory. A total of 12 composite plants from 2 independent transformation experiments were analyzed. (**D-E**) Images are maximum intensity projections and show merged fluorescent channels (Venus: green; mCherry: magenta; Calcofluor white cell-wall staining: grayscale in the upper panels). The Venus channel is shown in Green Fire Blue when isolated in lower panels, with blue or yellow indicating low or high fluorescence levels, respectively. The dotted-line ROIs indicate nuclei of infected cells (IC) from the C3 layer being passed by a cortical infection thread. The fluorescence intensity profiles of pCYCB1;2 and pKNOLLE reporter-associated signals along the green transects are shown in the corresponding right panels. NC: neighbouring cell. NOD: nodule primordium. Scale bars: 20 µm.

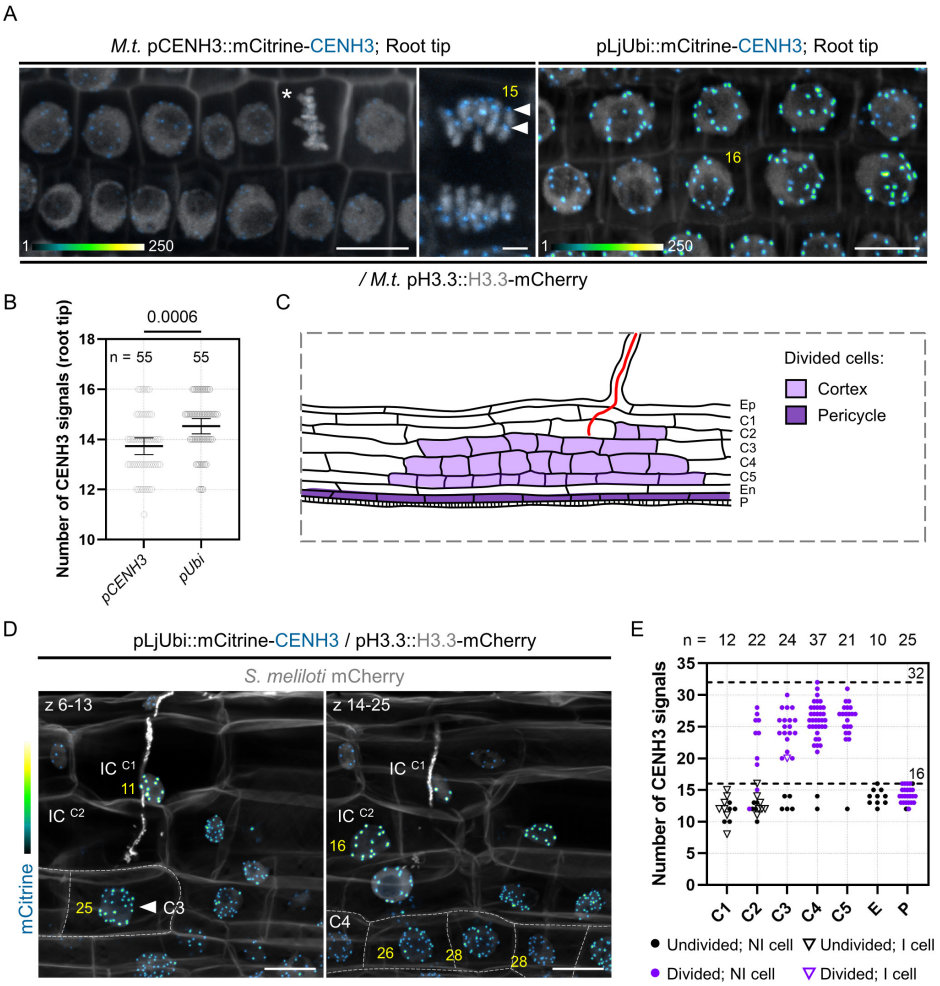

Figure 5. Dividing cortical cells initiating Medicago nodule primordium formation are tetraploid.
(**A**) Confocal images of whole-mount WT transgenic roots expressing mCitrine-CENH3 under the control of native (*M.t.* pCENH3; left and middle panels) or constitutive promoters (pLjUbi; right panel). Simultaneous expression of H3.3-mCherry enables the recognition of condensed (star) and segregating chromosomes (middle panel). mCitrine-CENH3 labels the centromeric region of individual chromosomes (filled arrowheads). The number of CENH3-labeled foci determined across image stacks is indicated in yellow. Images are maximum intensity projections and show merged fluorescent channels (mCitrine: Green Fire Blue; mCherry and Calcofluor white cell-wall staining: grayscale). In the Green Fire Blue colour scheme, blue or yellow indicate low or high fluorescence levels, respectively (min. to max. = 1-140 in the middle panel). Scale bars: left and right panels = 10 µm; middle panel = 2 µm. (**B**) Quantification of the number of centromeric signals in transgenic root tips expressing mCitrine-CENH3 under native (pCENH3) or constitutive (pUbi) promoters (n = 55 nuclei). All data points are shown and are from 2 (pUbi) to 3 (pCENH3) independent experiments with 7 composite plants analyzed per construct. Horizontal bars indicate sample means with 95% confidence interval. Differences were statistically significant (p-value = 0.0006) using a Mann-Whitney test. (**C**) Schematic representation of an early nodule primordium where anticlinal cell divisions occurred in the pericycle (P; dark violet) and cortical cells (C2 to C5; light violet). Rhizobia inside the infection thread are depicted in red. Ep: epidermis. En: endodermis. (**D**) Maximum intensity projections of an early nodule primodium at the developmental stage represented in (**C**), formed in a WT root expressing the pLjUbi::mCitrine-CENH3 / pH3.3::H3.3-mCherry construct at 7 dpi with mCherry-producing *S. meliloti*. Dotted-line ROIs indicate the contours of divided cells in the inner (C4) and middle (C3) cortical layers. The number of CENH3-labeled foci, determined across image stacks and indicated in yellow are: 11 and 16 in undivided, infected cells (IC) from the outer cortical layers (C1; left panel and C2, right panel) and 25 to 28 in divided, uninfected cells from the C3 (filled arrowhead; left panel) and C4 layers (right panel). Images show merged fluorescent channels (mCitrine: Green Fire Blue; mCherry and Calcofluor white cell-wall staining: grayscale). In the Green Fire Blue colour scheme, blue or yellow indicate low or high fluorescence levels, respectively. Scale bars: 20 µm. (**E**) Quantification of the number of centromeric signals in early nodule primordia at the developmental stage depicted in (**C**), formed in inoculated WT roots (7 to 12 dpi) constitutively expressing mCitrine-CENH3. The number (n) of analyzed nuclei in each cell layer is indicated on the top. E: endodermis. P: pericycle. All data points are shown with black or violet symbols indicating undivided or divided cells, respectively. NI: non-infected cell (discs). I: infected cell (triangles). Horizontal dotted lines are positioned at y = 16 and y = 32, corresponding to diploid (2n = 16) or tetraploid (4n = 32) cellular states in Medicago. Data are from 2 independent experiments with 7 nodule primordia from 5 composite plants analyzed.

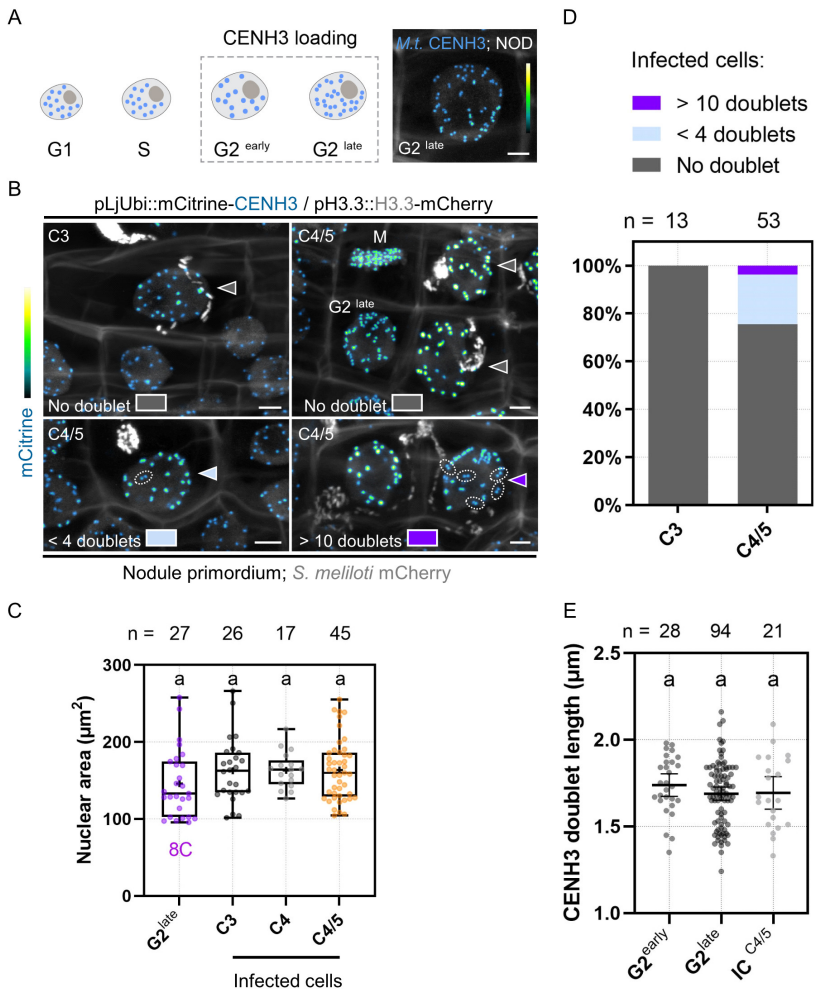

Figure 6. Primary infected nodule primordium cells do not reach full competence for chromosome segregation.
(**A**) Schematic representation of CENH3 deposition at centromeres (blue dots) throughout the different pre-mitotic (G1, S, G2 ^{early} and G2 ^{late}) cell-cycle phases in plants. Nuclei of increasing size and DNA content are depicted as ovals. The dotted-line frame indicates the timing of CENH3 loading at replicated centromeres, occurring during G2 before sister kinetochore (blue doublets) split in preparation to mitosis (Lermontova et al., 2007). Right panel: confocal image of a late G2-phase cell observed in a nodule (NOD) in an inoculated WT transgenic root (12 dpi) constitutively expressing mCitrine-CENH3. The majority of fluorescent signals appear as doublets corresponding to sister kinetochores. Scale bar: 5 µm. (**B**) Confocal images of whole-mount WT roots expressing the pLjUbi::mCitrine-CENH3 / pH3.3::H3.3-mCherry construct and inoculated with mCherry-producing *S. meliloti* (7 to 12 dpi). Filled arrowheads point to nuclei of infected nodule primordium cells. Dotted-line ROIs indicate mCitrine-CENH3 doublets appearing as twin spots on the same focal plane. Neighbouring cells in late G2 or undergoing mitosis (M) are indicated. The presence of CENH3-labeled twin spots was assessed across image stacks in the nuclei of infected cells from the middle (C3) and inner (C4/5) cortical layers and colour-coded as follows: grey = no doublet (upper panels); light blue = 1 to 3 doublets (lower left panel); dark violet = 11 or more doublets (lower right panel). Scale bars: 5 µm. (**A-B**) Images are maximum intensity projections (mCitrine: Green Fire Blue; mCherry and Calcofluor white cell-wall staining: grayscale). In the Green Fire Blue colour scheme, blue or yellow indicate low or high fluorescence levels, respectively. (**C**) Quantification of the nuclear area at the equatorial plane in cells being passed by a cortical infection thread (infected cells) in nodule primordia formed by WT transgenic roots inoculated with *S. meliloti* (7 to 12 dpi). The number (n) of analyzed nuclei in each cell layer (C3 to C4/5) is indicated on the top. The 8C chromatin-value is given for uninfected nodule primordium cells in late G2 showing close to 32 mCitrine-CENH3 doublets as identified in (**A**) and (**B**). All data points are shown and crosses indicate sample means. Differences were not statistically significant according to a Kruskal-Wallis test followed by Dunn's multiple comparisons test. At least 9 composite plants from 2 independent experiments were analyzed. (**D**) Quantification of infected cells in C3 (n = 13) and C4/5 (n = 53) cortical layers in nodule primordia, showing no doublet (grey), 1 to 3 doublets (light blue) or more than 11 doublets (dark violet) labelled by mCitrine-CENH3. Nine composite plants from 2 independent experiments were analyzed. (**E**) Quantification of the length of mCitrine-CENH3 doublets appearing as twin spots on the same focal plane in early G2 (n = 12), late G2-phase cells (n = 16) and infected cells (IC) from the C4/5 cortical layer (n = 13) in nodule primordia. n = 28 ($G2^{early}$), 94 ($G2^{late}$) and 21 (IC $^{C4/5}$) doublets. Horizontal bars indicate sample means with 95% confidence interval. Differences were not statistically significant according to a Kruskal-Wallis test followed by Dunn's multiple comparisons test. All data points are shown and are from 5 to 7 composite plants from 2 independent transformation experiments.

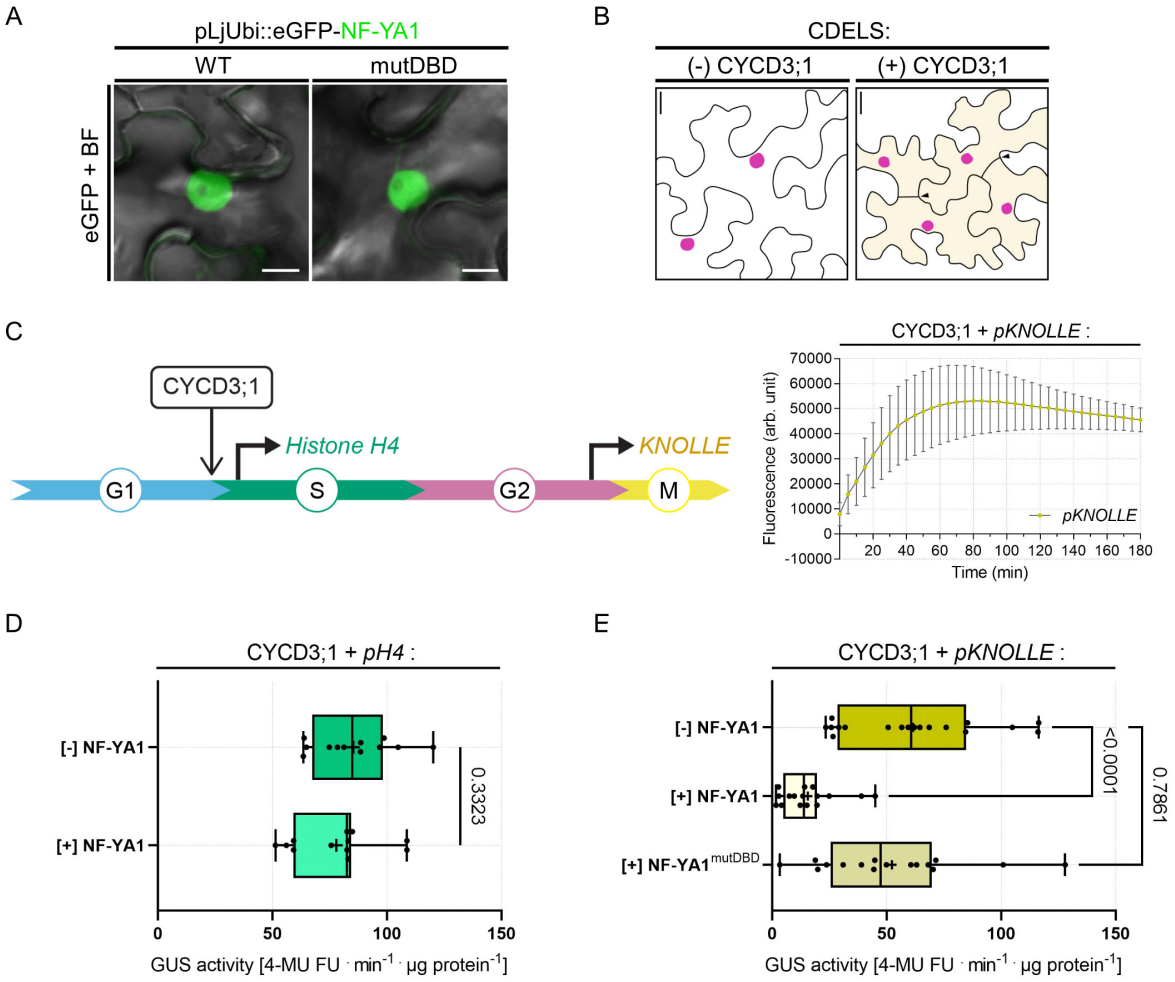

Figure 7. NF-YA1 specifically reduces the expression of a G2/M gene in a cell-division enabled system.
(**A**) Live-cell confocal images of *N. benthamiana* epidermal cells ectopically expressing eGFP-NF-YA1 variants: WT (left panel) or impaired in DNA recognition (mutDBD; right panel). Both fusion proteins accumulate in the nucleus and were used in fluorometric β-glucuronidase (GUS) assays. Images are maximum intensity projections and show merged fluorescent (eGFP: green) and bright field (BF) channels. Scale bars: 10 µm. (**B**) Schematic representation of the cell division-enabled leaf system (CDELS) on the scale of epidermal pavement cells in *N. benthamiana*. Differentiated cells in mature leaves (left panel) re-enter the canonical cell cycle upon ectopic expression of the Arabidopsis D-type cyclin CYCD3;1 (right panel). Nearly all re-activated pavement cells (diffuse yellow colouring) have completed cytokinesis after 3 days (filled arrowheads). See also Figure 7 – figure supplement 1B. Scale bars: 20 µm. (**C**) Left panel: schematic representation of the CDEL system on the scale of the canonical cell cycle. Ectopically-expressed CYCD3;1 targets and activates cyclin-dependent kinases (CDK, not shown), fostering the G1/S transition. Progression throughout the different cell-cycle phases is accompanied by the sequential activation of DNA synthesis (S) and mitotic genes (M). Histone *H4* and *KNOLLE* promoter-reporters were selected as readouts for G1/S and late G2/M transcriptional waves, respectively. Right panel: fluorometric GUS assay in tobacco leaf cells ectopically expressing CYCD3;1 and the Medicago pKNOLLE::GUS (*pKNOLLE*) reporter construct. Fluorescence curves (GUS-mediated hydrolysis of 4-MUG) over time are shown for 3 biological replicates. Error bars indicate standard deviation. Data are from 1 of 4 independent transient transformations. (**D**) Activity of GUS driven by the histone *H4* promoter (*pH4*) in the absence or presence of ectopically-expressed eGFP-NF-YA1 (NF-YA1) in CDEL samples (+ CYCD3;1). All data points are shown and crosses indicate sample means. Differences were not statistically significant (p-value = 0.3323) according to an unpaired t test with Welch's correction. Data are from 3 independent transformation experiments. n = 12 ([-] NF-YA1) and 12 ([+] NF-YA1) biological samples. (**E**) Activity of GUS driven by the *KNOLLE* promoter (*pKNOLLE*) in CDEL samples (+ CYCD3;1) in the absence or presence of ectopically-expressed eGFP-NF-YA1 variants with WT (NF-YA1) or mutated DNA-binding domain (NF-YA1^{mutDBD}). All data points are shown and crosses indicate sample means. Statistically significant differences ([-] NF-YA1 versus [+] NF-YA1; p-value < 0.0001) or non-significant differences ([-] NF-YA1 versus [+] NF-YA1^{mutDBD}; p-value = 0.7861) are based on a Kruskal-Wallis test followed by Dunn's multiple comparisons test. Data are from 4 to 5 independent transformation experiments. n = 18 ([-] NF-YA1), 16 ([+] NF-YA1), 16 ([+] NF-YA1^{mutDBD}) biological samples.

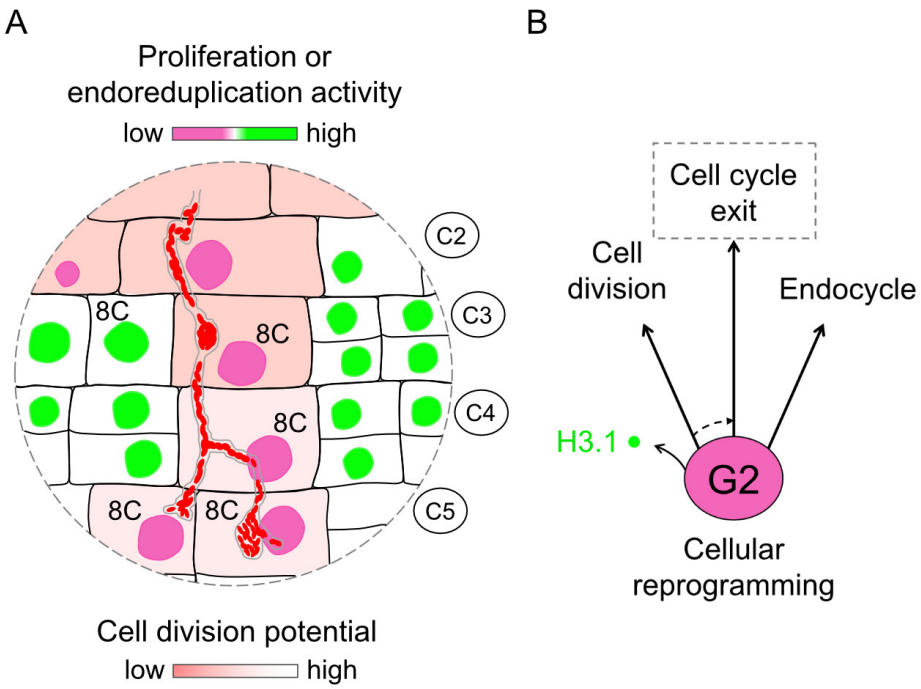

Figure 8. Model illustrating characteristic cellular traits on the cortical infection thread trajectory.
(**A**) Cortical cells competent for sustained transcellular infection thread progression are characterized by a reduced proliferation or endoreduplication activity (pink to green two-colour gradient). By the time they are crossed and ultimately internalize bacteria, such tetraploid cells (this study, Torrey and Barrios, 1969) reach a post-replicative, 8C ploidy stage but contrary to direct neighbour cells, they do not commit to a subsequent cell division (red to white two-colour gradient). (**B**) Rather, cells supporting transcellular infection presumably enter a prolonged G2-phase (this study, Yang et al., 1994) during which they remodel their histone H3 composition as part of their cellular reprogramming for infection. This differentiation process and concurrent transcellular passage are accomplished within a last cell-cycle round. We propose that cellular factors controlling the G2/M transition and eventually the exit from the canonical cell cycle (dashed arrow) are prominent candidates to support intracellular infection competence.